

A general framework for decomposing the phase field fracture driving force, particularised to a Drucker-Prager failure surface

Yousef Navidtehrani^a, Covadonga Betegón^a, Emilio Martínez-Pañeda^{b,*}

^a*Department of Construction and Manufacturing Engineering, University of Oviedo, Gijón 33203, Spain*

^b*Department of Civil and Environmental Engineering, Imperial College London, London SW7 2AZ, UK*

Abstract

Due to its computational robustness and versatility, the phase field fracture model has become the preferred tool for predicting a wide range of cracking phenomena. However, in its conventional form, its intrinsic tension-compression symmetry in damage evolution prevents its application to the modelling of compressive failures in brittle and quasi-brittle solids, such as concrete or rock materials. In this work, we present a general methodology for decomposing the phase field fracture driving force, the strain energy density, so as to reproduce asymmetrical tension-compression fracture behaviour. The generalised approach presented is particularised to the case of linear elastic solids and the Drucker-Prager failure criterion. The ability of the presented model to capture the compressive failure of brittle materials is showcased by numerically implementing the resulting strain energy split formulation and addressing four case studies of particular interest. Firstly, insight is gained into the capabilities of the model in predicting friction and dilatancy effects under shear loading. Secondly, virtual direct shear tests are conducted to assess fracture predictions under different pressure levels. Thirdly, a concrete cylinder is subjected to uniaxial and triaxial compression to investigate the influence of confinement. Finally, the localised failure of a soil slope is predicted and the results are compared with other formulations for the strain energy decomposition proposed in the literature. The results provide a good qualitative agreement with experimental observations and demonstrate the capabilities of phase field fracture methods to predict crack nucleation and growth under multi-axial loading in materials exhibiting asymmetric tension-compression fracture behaviour.

Keywords:

Phase field fracture, Fracture driving force, Brittle fracture, Drucker-Prager criterion, Strain energy split

*Corresponding author.

Email address: e.martinez-paneda@imperial.ac.uk (Emilio Martínez-Pañeda)

1. Introduction

The application of the phase field paradigm to fracture mechanics has enabled predicting cracking phenomena of arbitrary complexity [1, 2]. These include not only hitherto complex crack trajectories but also crack branching, nucleation and merging, without *ad hoc* criteria and cumbersome tracking techniques, in both two and three dimensions [3, 4]. In phase field methods, the crack-solid interface is not explicitly modelled but instead smeared over a finite domain and characterised by an auxiliary phase field variable ϕ , which takes two distinct values in each of the phases (e.g., $\phi = 0$ in intact material points and $\phi = 1$ inside of the crack). Hence, interfacial boundary conditions are replaced by a differential equation that describes the evolution of the phase field ϕ . Phase field fracture methods have become the *de facto* choice for modelling a wide range of cracking phenomena. New phase field formulations have been presented for ductile fracture [5, 6], composite materials [7–9], shape memory alloys [10, 11], functionally graded materials [12, 13], fatigue damage [14, 15] and hydrogen embrittlement [16, 17], among others (see Refs. [18, 19] for an overview).

Most frequently, the phase field is defined to evolve in agreement with Griffith’s energy balance [20] - crack growth is predicted by the exchange between elastic and fracture energies. While thermodynamically rigorous, this leads to a symmetric fracture behaviour in tension and compression, implying that crack interpenetration can occur in compressive stress states, and that the compressive strength is assumed to be equal to the tensile strength. In metals, which often fail in compression by buckling, crumbling or 45-degree shearing, this leads to nonphysical predictions of crack nucleation in compressive regions, such as the vicinity of loading pins in standardised experiments like three-point bending or compact tension. For brittle and quasi brittle solids, such as concrete or geomaterials, the assumption of tension-compression symmetry is unrealistic as compressive-to-tensile strength ratios typically range between $\sigma_c/\sigma_t = 2$ and $\sigma_c/\sigma_t = 25$ [21]. In brittle materials, compressive failure takes place due to the linkage of pre-existing micro-cracks growing under local tensile stresses [22], while tensile brittle fractures are typically due to unstable crack propagation. Thus, extending the use of phase field to the prediction of compressive failures in brittle solids requires the development of new formulations that can accommodate appropriate failure surfaces. To achieve this goal, we here present a general approach for decomposing the phase field fracture driving force, the strain energy density. We then particularise such approach to the case of a Drucker-Prager failure surface and

numerically show that it can adequately capture cracking patterns in concrete and geomaterials.

2. The variational phase field fracture framework

We shall begin by providing a brief introduction to the variational phase field fracture formulation; the reader is referred to Ref. [1] for a comprehensive description. Considering a body Ω with a crack surface Γ , where the displacement field \mathbf{u} might be discontinuous, the energy functional can be formulated as the sum of the elastic energy stored in the cracked body and the energy required to grow the crack [23]:

$$\mathcal{E} = \int_{\Omega} \psi(\boldsymbol{\varepsilon}(\mathbf{u})) \, dV + \int_{\Gamma} G_c \, d\Gamma, \quad (1)$$

where ψ is the elastic strain energy density, which is a function of the strain tensor $\boldsymbol{\varepsilon}(\mathbf{u})$, and G_c is a measure of the energy required to create two new surfaces, the material toughness. Equation (1) postulates Griffith's minimality principle in a global manner and its minimisation enables predicting arbitrary cracking phenomena solely as a result of the exchange between elastic and fracture energies. However, minimising Griffith's functional \mathcal{E} is hindered by the unknown nature of the crack surface Γ . This can be overcome by the use of the phase field paradigm; diffusing the interface over a finite region and tracking its evolution by means of an auxiliary phase field variable ϕ . Accordingly, Eq. (1) can be approximated by the following regularised functional:

$$\mathcal{E}_\ell = \int_{\Omega} g(\phi) \psi_0(\boldsymbol{\varepsilon}(\mathbf{u})) \, dV + \int_V G_c \gamma(\phi, \nabla\phi, \ell) \, dV, \quad (2)$$

where ψ_0 denotes the elastic strain energy density of the undamaged solid, $g(\phi)$ is a degradation function to reduce the stiffness of the solid with increasing damage, and $\gamma(\phi, \nabla\phi, \ell)$ is the so-called crack density function. For simplicity, and without loss of generality, we adopt the constitutive choices of the so-called conventional or AT2 phase field model [24], such that

$$g(\phi) = (1 - \phi)^2 \quad \text{and} \quad \gamma(\phi, \nabla, \ell\phi) = \frac{1}{2\ell}\phi^2 + \frac{\ell}{2}|\nabla\phi|^2 \quad (3)$$

where ℓ is the phase field length scale, inherently arising due to the non-local nature of the model. The strong form of the balance equations can be derived by taking the first variation of \mathcal{E}_ℓ with respect to the primal kinematic variables (\mathbf{u}, ϕ) and making use of Gauss' divergence theorem, rendering

$$\begin{aligned} \nabla \cdot [(1 - \phi)^2 \boldsymbol{\sigma}_0] &= \mathbf{0} \quad \text{in } \Omega \\ G_c \left(\frac{\phi}{\ell} - \ell \nabla^2 \phi \right) - 2(1 - \phi) \psi_0 &= 0 \quad \text{in } \Omega \end{aligned} \quad (4)$$

where $\boldsymbol{\sigma}_0$ is the undamaged stress tensor. As seen in (4)b, the evolution of the phase field is governed by the (undamaged) elastic strain energy density which, for linear elastic isotropic solids, is given by

$$\psi_0 = \frac{1}{2} \lambda \text{tr}(\boldsymbol{\varepsilon})^2 + \mu \boldsymbol{\varepsilon} : \boldsymbol{\varepsilon}, \quad (5)$$

where λ and μ are the Lamé coefficients. It follows that the phase field is insensitive to the compressive or tensile nature of the mechanical fields (tension-compression symmetry in damage evolution). To enforce a distinction between tension and compression behaviour, several formulations have been proposed. Initially, the motivation was the need to avoid crack interpenetration and achieve the resistance to cracking under compression observed in some materials such as metals. Examples of strain energy decompositions formulated with this objective include the volumetric-deviatoric split by Amor *et al.* [25], the spectral decomposition by Miehe and co-workers [26], and the purely tensile splits (so-called 'no-tension' models) of Freddi and Royer-Carfagni [27, 28] and Lo *et al.* [29]. On the other hand, rising interest in using phase field methods to model fracture in concrete and geomaterials has led to the development of driving force definitions that accommodate non-symmetric failure surfaces [30]. Zhou *et al.* [31] and Wang *et al.* [32] developed new driving force formulations based on Mohr-Coulomb theory. And very recently, de Lorenzis and Maurini [33] presented an analytical study where the strain energy split was defined based on a Drucker-Prager failure surface. The majority of these works adopt the following structure. The elastic strain energy density is decomposed into two parts: (i) a part affected by damage, ψ_d , and (ii) a stored residual elastic part ψ_s , which is independent of the damage variable and thus not susceptible to dissipation. Accordingly,

$$\psi_0(\boldsymbol{\varepsilon}) = \psi_d(\boldsymbol{\varepsilon}) + \psi_s(\boldsymbol{\varepsilon}), \quad \text{and} \quad \psi(\boldsymbol{\varepsilon}, \phi) = g(\phi) \psi_d(\boldsymbol{\varepsilon}) + \psi_s(\boldsymbol{\varepsilon}), \quad (6)$$

which necessarily implies,

$$\psi(\boldsymbol{\varepsilon}, \phi) = g(\phi) \psi_0(\boldsymbol{\varepsilon}) + (1 - g(\phi)) \psi_s(\boldsymbol{\varepsilon}). \quad (7)$$

And this decomposition of the strain energy density gives rise to an analogous decomposition of the Cauchy stress tensor, such that

$$\boldsymbol{\sigma}(\boldsymbol{\varepsilon}, \phi) = g(\phi) \frac{\partial \psi_d(\boldsymbol{\varepsilon})}{\partial \boldsymbol{\varepsilon}} + \frac{\partial \psi_s(\boldsymbol{\varepsilon})}{\partial \boldsymbol{\varepsilon}} = g(\phi) \boldsymbol{\sigma}^d + \boldsymbol{\sigma}^s. \quad (8)$$

where $\boldsymbol{\sigma}^d$ and $\boldsymbol{\sigma}^s$ respectively denote the damaged and non-degraded parts of the Cauchy stress tensor.

The aim of this work is to present a generalised approach to identify $\psi_s(\boldsymbol{\varepsilon})$ (and subsequently $\psi_d(\boldsymbol{\varepsilon})$) as a function of the failure surface and the constitutive behaviour of the pristine material.

This is presented below, in Section 3, where the framework is exemplified with a Drucker-Prager [34] failure surface.

3. A general approach for decomposing the strain energy density based on failure criteria

We proceed to present a general approach for decomposing the strain energy density so as to incorporate any arbitrary failure criterion in the phase field fracture method. As the strain energy density is the driving force for fracture, a suitable choice of strain energy decomposition can enable reproducing the desired failure surface. Such a choice must satisfy the failure criterion assumed while recovering the constitutive behaviour of the pristine material. Here, for simplicity, we choose to focus on solids exhibiting linear elastic behaviour in the undamaged state. However, the framework is general and can be extended to other constitutive responses, such as hyperelasticity. We shall first derive the partial differential equation (PDE) that characterises the possible solutions for the non-dissipative stored strain energy density ψ_s in linear elastic solids. Then, we consider the failure envelope function that provides the constraint required to obtain a solution to this PDE. The process is exemplified with a Drucker-Prager failure surface, and the section concludes with brief details of the numerical implementation.

As in Ref. [27], the *Theory of Structured Deformations* [35] is applied to a damaged continuum solid. We confine our attention to infinitesimal deformations, such that the total strain tensor can be estimated from the displacement vector as,

$$\boldsymbol{\varepsilon} = \frac{1}{2} (\nabla \mathbf{u}^T + \nabla \mathbf{u}) \quad (9)$$

A Representative Volume Element (RVE) can be defined, see Fig. 1, such that the meso-scale representation of the material involves regions of intact material and micro-cracks. In this context, the phase field ϕ is akin to a damage variable, and describes the integrity of the RVE (the extent of dominance of intact and cracked regions, within the two limiting cases of $\phi = 0$ and $\phi = 1$). The macroscopic deformation is then the sum of two contributions: an elastic straining of the intact material regions, and the opening and sliding of micro-cracks, that can coalesce into macroscopic cracks. Accordingly,

$$\boldsymbol{\varepsilon} = \boldsymbol{\varepsilon}^e + \boldsymbol{\varepsilon}^d, \quad (10)$$

where $\boldsymbol{\varepsilon}^e$ are the elastic (recoverable) strains due to the deformation of the undamaged structure, while $\boldsymbol{\varepsilon}^d$ denotes the inelastic strains associated with microscopic damage mechanisms.

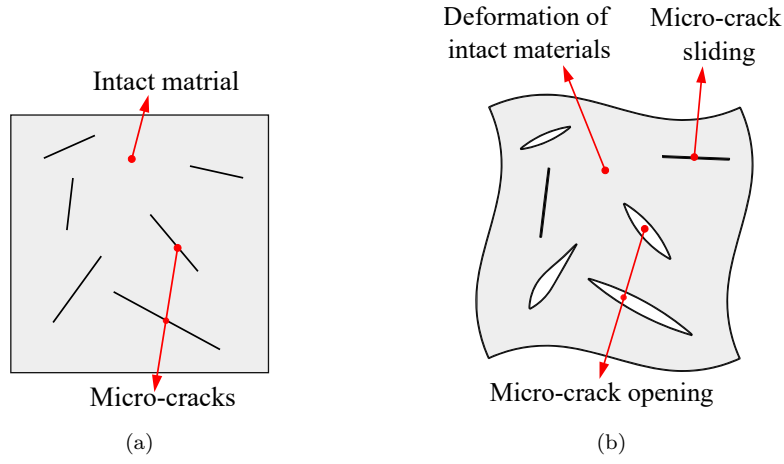


Figure 1: Meso-scale Representative Volume Element (RVE) of a damaged solid, showing regions of micro-cracks and intact material in the: (a) undeformed, and (b) deformed states, with the latter emphasising the effect of micro-crack opening and sliding.

The elastic strain tensor $\boldsymbol{\varepsilon}^e$ is related to the Cauchy stress tensor through the inverse of the elastic stiffness matrix $\boldsymbol{\varepsilon}^e = (\mathcal{C}_0)^{-1} \boldsymbol{\sigma}$ and, if $\boldsymbol{\varepsilon}^e$ and $\boldsymbol{\varepsilon}^d$ are orthogonal, the stored and damaged strain energy densities of effective configuration (see Section 2) can be estimated as,

$$\psi_s = \frac{1}{2} \boldsymbol{\varepsilon}^e C_0 \boldsymbol{\varepsilon}^e \quad \text{and} \quad \psi_d = \frac{1}{2} \boldsymbol{\varepsilon}^d C_0 \boldsymbol{\varepsilon}^d \quad (11)$$

with the total strain energy density ψ being computed from ψ_s and ψ_d using Eq. (6). Now, let us consider the strain energy density of pristine material as a function of the effective stress invariants ($I_1(\boldsymbol{\sigma}_0), J_2(\boldsymbol{\sigma}_0)$);

$$\psi_0(\boldsymbol{\varepsilon}) = \frac{1}{18K} I_1^2(\boldsymbol{\sigma}_0(\boldsymbol{\varepsilon})) + \frac{1}{2\mu} J_2(\boldsymbol{\sigma}_0(\boldsymbol{\varepsilon})), \quad (12)$$

where K is the bulk modulus, μ is the shear modulus, I_1 is the first invariant of a tensor, and J_2 is the second invariant of the deviatoric part of a tensor. Eq. (12) holds for any linear elastic isotropic solid. The stiffness and material behaviour associated with the non-degraded strain energy density ψ^s and stress $\boldsymbol{\sigma}^s$ corresponds to that of intact material and, accordingly,

$$\psi_s = \frac{1}{18K} I_1^2(\boldsymbol{\sigma}^s) + \frac{1}{2\mu} J_2(\boldsymbol{\sigma}^s). \quad (13)$$

Then, for any choice of $\psi(I_1(\boldsymbol{\varepsilon}), J_2(\boldsymbol{\varepsilon}))$, it is possible to describe the relation between the invariants of strain and stress as follows (see Appendix A):

$$I_1(\boldsymbol{\sigma}(\boldsymbol{\varepsilon})) = 3 \frac{\partial \psi(\boldsymbol{\varepsilon})}{\partial I_1(\boldsymbol{\varepsilon})}, \quad J_2(\boldsymbol{\sigma}(\boldsymbol{\varepsilon})) = J_2(\boldsymbol{\varepsilon}) \left(\frac{\partial \psi(\boldsymbol{\varepsilon})}{\partial J_2(\boldsymbol{\varepsilon})} \right)^2 \quad (14)$$

By substituting Eq. (14) into Eq. (13), one can obtain the PDE for the stored strain energy density,

$$\psi_s = \frac{1}{2K} \left(\frac{\partial \psi_s}{\partial I_1(\boldsymbol{\varepsilon})} \right)^2 + \frac{J_2(\boldsymbol{\varepsilon})}{2\mu} \left(\frac{\partial \psi_s}{\partial J_2(\boldsymbol{\varepsilon})} \right)^2 \quad (15)$$

Upon the appropriate constraints and boundary conditions, one can solve the PDE (15) to obtain the non-dissipative stored part of the strain energy density for any level of material damage. The additional constraint needed comes from the definition of the failure criterion under consideration. Any arbitrary failure envelope can be defined in terms of the stress invariants for the fully damaged state. For illustration, let us consider a failure surface defined in terms of I_1 and J_2 ; i.e., $f(I_1(\boldsymbol{\sigma}^f), J_2(\boldsymbol{\sigma}^f)) = 0$, where $\boldsymbol{\sigma}^f = \boldsymbol{\sigma}(\boldsymbol{\varepsilon}, \phi = 1)$. Accordingly, considering Eq. (14), the following failure envelope function can be defined:

$$f \left(\frac{\partial \psi_s(\boldsymbol{\varepsilon})}{\partial I_1(\boldsymbol{\varepsilon})}, \frac{\partial \psi_s(\boldsymbol{\varepsilon})}{\partial J_2(\boldsymbol{\varepsilon})} \right) = 0 \quad (16)$$

and ψ_s can be found from the common solution to Eqs. (15) and (16) upon the application of appropriate boundary conditions. This is showcased below for a Drucker-Prager failure envelope.

3.1. Particularisation to the Drucker-Prager failure surface

Drucker-Prager's failure criterion was developed for pressure-dependent materials like rock, concrete, foams and polymers. In terms of invariants of stress, the Drucker-Prager criterion is expressed as follows,

$$\sqrt{J_2(\boldsymbol{\sigma})} = A + BI_1(\boldsymbol{\sigma}), \quad (17)$$

where A and B are a function of the uniaxial tensile (σ_t) and compressive (σ_c) strengths, such that

$$A = \frac{2}{\sqrt{3}} \left(\frac{\sigma_c \sigma_t}{\sigma_c + \sigma_t} \right); \quad B = \frac{1}{\sqrt{3}} \left(\frac{\sigma_t - \sigma_c}{\sigma_c + \sigma_t} \right). \quad (18)$$

A material point sitting inside the Drucker-Prager failure envelope can be assumed to behave in a linear elastic manner, with damage-driven non-linear behaviour being triggered when the stress state reaches the failure surface. Assuming that the same degradation function $g(\phi)$ applies to the tensile and compressive strengths, then the sensitivity of the parameters A and B to the phase field variable is characterised by,

$$\begin{aligned} A(\phi) &= \frac{2}{\sqrt{3}} \left(\frac{g(\phi)\sigma_c g(\phi)\sigma_t}{g(\phi)\sigma_c + g(\phi)\sigma_t} \right) = g(\phi) \frac{2}{\sqrt{3}} \left(\frac{\sigma_c \sigma_t}{\sigma_c + \sigma_t} \right) = g(\phi) A(\phi = 0) \\ B(\phi) &= \frac{1}{\sqrt{3}} \left(\frac{g(\phi)\sigma_t - g(\phi)\sigma_c}{g(\phi)\sigma_c + g(\phi)\sigma_t} \right) = \frac{1}{\sqrt{3}} \left(\frac{\sigma_t - \sigma_c}{\sigma_c + \sigma_t} \right) = B(\phi = 0) \end{aligned} \quad (19)$$

Accordingly, for the fully damaged state ($\phi = 1$), the Drucker-Prager parameters read,

$$A(\phi = 1) = 0; \quad B(\phi = 1) = B(\phi = 0). \quad (20)$$

I.e., A is degraded as the phase field evolves, while the parameter B is insensitive to the damage state. This can be physically interpreted through the cohesion parameter c and the friction angle θ of Mohr-Coulomb's criterion, and their relationship with Drucker-Prager's coefficients:

$$A(\theta, c) = \frac{6c \cos \theta}{\sqrt{3}(3 + \sin \theta)}; \quad B(\theta) = \frac{2 \sin \theta}{\sqrt{3}(3 + \sin \theta)}. \quad (21)$$

As seen in Eq. (21), B is only a function of the friction angle, while A is also a function of c , exhibiting a linear relationship with the cohesion parameter. Since damage translates into a loss of cohesion, both A and c degrade with evolving damage, and eventually vanish in fully cracked state.

In addition, consistent with Eq. (17), the stress state in the fully damaged configuration satisfies,

$$\sqrt{J_2(\boldsymbol{\sigma}^f)} = BI_1(\boldsymbol{\sigma}^f), \quad (22)$$

as the stress state goes back to the failure envelope for $\phi = 1$ (see Fig. 2).

As discussed above, our general approach requires a function describing the failure condition in terms of the strain energy density and the strains - see Eq. (16). This can be achieved by combining Eqs. (14) and (22), reaching

$$f\left(\frac{\partial \psi_s(\boldsymbol{\varepsilon})}{\partial I_1(\boldsymbol{\varepsilon})}, \frac{\partial \psi_s(\boldsymbol{\varepsilon})}{\partial J_2(\boldsymbol{\varepsilon})}\right) = \sqrt{J_2(\boldsymbol{\varepsilon})} \frac{\partial \psi_s(\boldsymbol{\varepsilon})}{\partial J_2(\boldsymbol{\varepsilon})} - 3B \frac{\partial \psi_s(\boldsymbol{\varepsilon})}{\partial I_1(\boldsymbol{\varepsilon})} = 0 \quad (23)$$

An isotropic linear elastic material must satisfy Eq. (15) and, if obeying the Drucker-Prager failure criterion, also Eq. (23). Hence, the common solution to these two PDEs will give us the stored (elastic) strain energy density ψ_s . Let us obtain this common solution by first finding the general solution of Eq. (23), which is of the form

$$\psi_s = a_1 \left(I_1(\boldsymbol{\varepsilon}) + 6B\sqrt{J_2(\boldsymbol{\varepsilon})} \right)^2 + a_2 \quad (24)$$

where a_1 and a_2 are unknowns. These can be estimated by applying suitable boundary conditions and substituting the general solution into the second PDE. Hence, considering the boundary condition $\psi_s(I_1(\boldsymbol{\varepsilon}) = 0, J_2(\boldsymbol{\varepsilon}) = 0) = 0$, one finds that $a_2 = 0$. Then, the remaining unknown is obtained by deriving Eq. (24) with respect to $I_1(\boldsymbol{\varepsilon})$ and $J_2(\boldsymbol{\varepsilon})$ and substituting into Eq. (15), rendering

$$a_1 = \frac{K\mu}{18B^2K + 2\mu}. \quad (25)$$

Accordingly, upon substitution in Eq. (24), the stored (elastic) strain energy density associated with the Drucker-Prager failure envelope is found to be:

$$\psi_s = \frac{K\mu}{18B^2K + 2\mu} \left(I_1(\boldsymbol{\varepsilon}) + 6B\sqrt{J_2(\boldsymbol{\varepsilon})} \right)^2 \quad (26)$$

However, one should note that Eq. (26) is only valid for stress states that are above the failure envelope. Three potential scenarios exist: (1) the first invariant of stress is positive, $I_1(\boldsymbol{\sigma}) > 0$; (2) the stress state is above the failure criterion, $\sqrt{J_2(\boldsymbol{\sigma})} \geq BI_1(\boldsymbol{\sigma})$; and (3) the stress state is below the failure criterion, $\sqrt{J_2(\boldsymbol{\sigma})} < BI_1(\boldsymbol{\sigma})$. With scenarios (2) and (3) being only relevant when $I_1(\boldsymbol{\sigma}) < 0$. We then proceed to generalise Eq. (26) to encompass those three regimes (see Appendix B), such that

$$\psi_s = \begin{cases} 0 & \text{for } -6B\sqrt{J_2(\boldsymbol{\varepsilon})} < I_1(\boldsymbol{\varepsilon}) \\ \frac{K\mu}{18B^2K + 2\mu} \left(I_1(\boldsymbol{\varepsilon}) + 6B\sqrt{J_2(\boldsymbol{\varepsilon})} \right)^2 & \text{for } -6B\sqrt{J_2(\boldsymbol{\varepsilon})} \geq I_1(\boldsymbol{\varepsilon}) \ \& \ 2\mu\sqrt{J_2(\boldsymbol{\varepsilon})} \geq 3BK I_1(\boldsymbol{\varepsilon}) \\ \frac{1}{2}KI_1^2(\boldsymbol{\varepsilon}) + 2\mu J_2(\boldsymbol{\varepsilon}) & \text{for } 2\mu\sqrt{J_2(\boldsymbol{\varepsilon})} < 3BK I_1(\boldsymbol{\varepsilon}) \end{cases} \quad (27)$$

And the damaged part of the strain energy density can be readily estimated using Eq. (6), rendering

$$\psi_d = \begin{cases} \frac{1}{2}KI_1^2(\boldsymbol{\varepsilon}) + 2\mu J_2(\boldsymbol{\varepsilon}) & \text{for } -6B\sqrt{J_2(\boldsymbol{\varepsilon})} < I_1(\boldsymbol{\varepsilon}) \\ \frac{1}{18B^2K + 2\mu} \left(-3BK I_1(\boldsymbol{\varepsilon}) + 2\mu\sqrt{J_2(\boldsymbol{\varepsilon})} \right)^2 & \text{for } -6B\sqrt{J_2(\boldsymbol{\varepsilon})} \geq I_1(\boldsymbol{\varepsilon}) \ \& \ 2\mu\sqrt{J_2(\boldsymbol{\varepsilon})} \geq 3BK I_1(\boldsymbol{\varepsilon}) \\ 0 & \text{for } 2\mu\sqrt{J_2(\boldsymbol{\varepsilon})} < 3BK I_1(\boldsymbol{\varepsilon}) \end{cases} \quad (28)$$

The different stress states are illustrated in Fig. 2 in terms of their location in the $(I_1(\boldsymbol{\sigma}), \sqrt{J_2(\boldsymbol{\sigma})})$ space, where the colour contours denote the magnitude of the total strain energy (increasing as we move away from the origin). The loading path illustrated with blue dots, path (a), illustrates the case where the first invariant of stress is positive $I_1(\boldsymbol{\sigma}) > 0$. In such a scenario, the failure process is driven by ψ_d , with the fully damage state achieved by returning to the origin (where the loading path intersects the Drucker-Prager failure criterion). In regards to the stress states on the left side of the figure ($I_1(\boldsymbol{\sigma}) < 0$), their behaviour is differentiated by their location relative to the Drucker-Prager criterion, which is represented by the $\sqrt{J_2(\boldsymbol{\sigma})} = BI_1(\boldsymbol{\sigma})$ line. Thus, the red loading path (b) is above the Drucker-Prager criterion and both ψ_s and ψ_c are active, see Eqs. (27)b and (28)b. Eventually, the loading path intersects again the $\sqrt{J_2(\boldsymbol{\sigma})} = BI_1(\boldsymbol{\sigma})$ line, reaching the fully damaged state and the associated residual strain energy density ψ_s . Finally, loading paths within the $I_1(\boldsymbol{\sigma}) < 0$ domain can also lie below the failure criterion, as showcased by the purple circles, path (c). In this case,

$\psi_d = 0$, see Eq. (28)c, and consequently $\phi = 0$. As shown in Fig. 2, changes in stress state associated with the loading path might lead to an intersection with the Drucker-Prager failure line, in what would constitute a micro-fracturing nucleation event ($\phi > 0$). Subsequently, final rupture ($\phi = 1$) would be attained when the loading path intersects again with the failure line, rendering a residual strain energy density ψ_s .

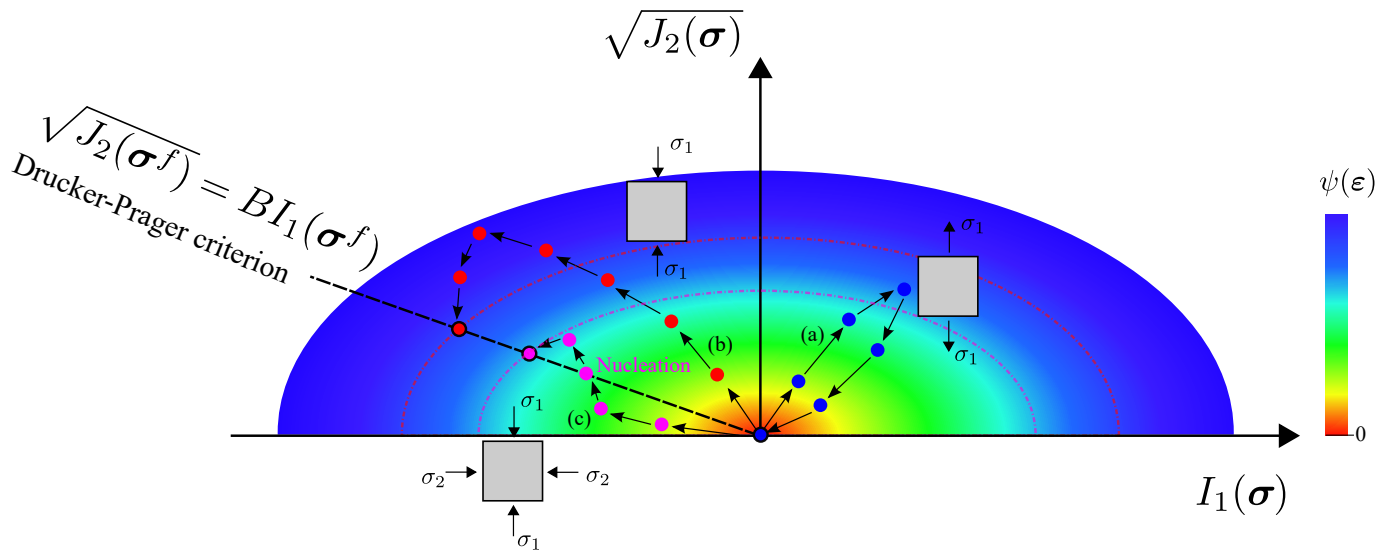


Figure 2: Stress states in the $(I_1(\boldsymbol{\sigma}), \sqrt{J_2(\boldsymbol{\sigma})})$. Three loading paths have been schematically incorporated to showcase the three potential scenarios discussed in Eqs. (27) and (28), and colour contours denote the magnitude of the total strain energy (increasing as we move away from the origin). Circles with an outer black domain denote fully damaged states ($\phi = 1$).

This phase field fracture formulation built upon Drucker-Prager’s failure criterion is numerically implemented using the finite element method. Retaining unconditional stability, we solve in a monolithic fashion the coupled system of equations that results from restating the local force balances,

$$\begin{aligned} \nabla \cdot \left[(1 - \phi)^2 \frac{\partial \psi_d(\boldsymbol{\varepsilon})}{\partial \boldsymbol{\varepsilon}} + \frac{\partial \psi_s(\boldsymbol{\varepsilon})}{\partial \boldsymbol{\varepsilon}} \right] &= \mathbf{0} \quad \text{in } \Omega \\ G_c \left(\frac{\phi}{\ell} - \ell \nabla^2 \phi \right) - 2(1 - \phi) \mathcal{H} &= 0 \quad \text{in } \Omega \end{aligned} \quad (29)$$

into their weak form. Here, $\mathcal{H} = \max \psi_d(t)$ is a history field introduced to enforce damage irreversibility [26]. As described in Appendix C, we take advantage of the analogy between the phase field evolution law and the heat transfer equation to implement the model into the finite element package ABAQUS using solely a user-material subroutine (UMAT) (see Refs. [36, 37]).

4. Representative results

Now, we shall illustrate the potential of enriching the phase field fracture description with a failure envelope of our choice. Specifically, through numerical examples, we will showcase how a formulation based on the Drucker-Prager failure criterion can capture the compressive failure of brittle materials such as concrete or geomaterials, along with capturing frictional behaviour and the dilatancy effect. Firstly, in Section 4.1, we gain insight into the material behaviour resulting from the Drucker-Prager strain energy split adopted by investigating the response of a single element undergoing shear. Secondly, numerical experiments using the Direct Shear Test (DST) configuration are conducted in Section 4.2. The goal is to investigate the fracture predictions obtained under the conditions relevant to the determination of the failure properties of frictional materials. The third case study, shown in Section 4.3, involves conducting virtual uniaxial and triaxial compression tests on concrete, so as to investigate the confinement effect. Finally, in Section 4.4, the predictions obtained from three strain energy splits are compared in the modelling of the localised failure of a soil slope. Our finite element calculations extend the very recent analytical study by de Lorenzis and Maurini [33], where a Drucker-Prager failure surface was also adopted.

4.1. Single element under shear deformation

We begin our numerical experiments by conducting shear tests on a single element. The aim is to investigate the ability of the Drucker-Prager based formulation presented in capturing frictional behaviour and the dilatancy effect. The latter is the volume change observed in granular materials subjected to shear deformations, due to the interlocking between grains and interfaces (see Fig. 3).

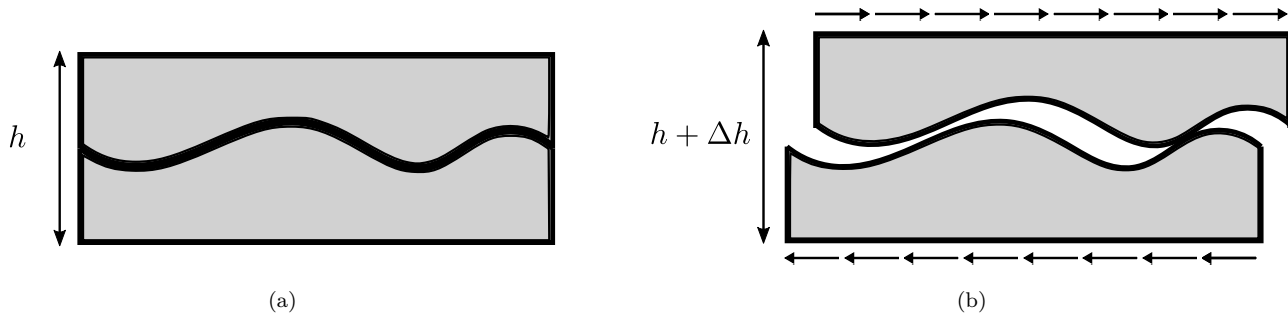


Figure 3: Sketch showcasing the dilatancy effect on geomaterials, also known as Reynolds dilatancy. Bulk expansion takes place due to the lever motion that occurs between neighbouring grains as a result of interlocking.

As shown in Fig. 4, a single plane strain element is considered undergoing both shear and uniaxial pressure. Specifically, a vertical constant pressure is first applied, followed by shear displacement at

the top and bottom edges. In this and all other case studies, the Neumann boundary condition $\nabla\phi \cdot \mathbf{n} = 0$ is adopted for the phase field. The constitutive behaviour of the element is characterised by linear elasticity, with a Young's modulus of $E = 25$ GPa and a Poisson's ratio of $\nu = 0.2$. The fracture behaviour is described by a material toughness of $G_c = 0.15$ kJ/m² and a phase field length scale of $\ell = 2$ mm.

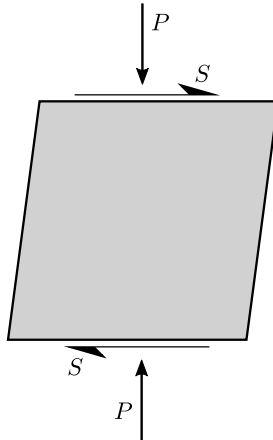


Figure 4: Configuration of a single element under pressure and shear stress.

We aim at assessing the frictional behaviour of the model, for which it is convenient to formulate the relation between the shear strain ε_{xy} and the shear stress σ_{xy} , as a function of the pressure and Drucker-Prager's B parameter. For the fully damaged state ($\phi = 1$), this relation reads

$$(\sigma_f)_{xy} = \frac{\partial\psi_c(\boldsymbol{\varepsilon})}{\partial\varepsilon_{xy}} = \frac{K\mu}{9B^2K + \mu} \left(\frac{I_1(\boldsymbol{\varepsilon})}{\sqrt{J_2(\boldsymbol{\varepsilon})}} + 6B \right) \varepsilon_{xy} \quad (30)$$

First, let us consider the case of no pressure ($P = 0$). Fig. 5a shows the shear stress versus shear strain curves obtained for different B values. The role played by damage evolution can be readily observed, with calculations obtained for low absolute B values exhibiting a peak in the shear stress response. For the fully cracked state ($\phi = 1$), the shear stress drops to zero only if $B = 0$. Hence, the expected influence of dilatancy on the stress-strain curve is attained for $B \neq 0$, and the effect increases with increasing its absolute magnitude ($|B|$). This load bearing capacity that is retained after reaching the fully cracked state due to dilatancy arises due to two contributions. One is the term $6B$ in Eq. (30). The second one is the term $I_1(\boldsymbol{\varepsilon})/\sqrt{J_2(\boldsymbol{\varepsilon})}$ - as shown in Fig. 5b, it attains a positive constant value for $\phi = 1$ and $B \neq 0$. However, the relation between B and $I_1(\boldsymbol{\varepsilon})/\sqrt{J_2(\boldsymbol{\varepsilon})}$ is non-linear.

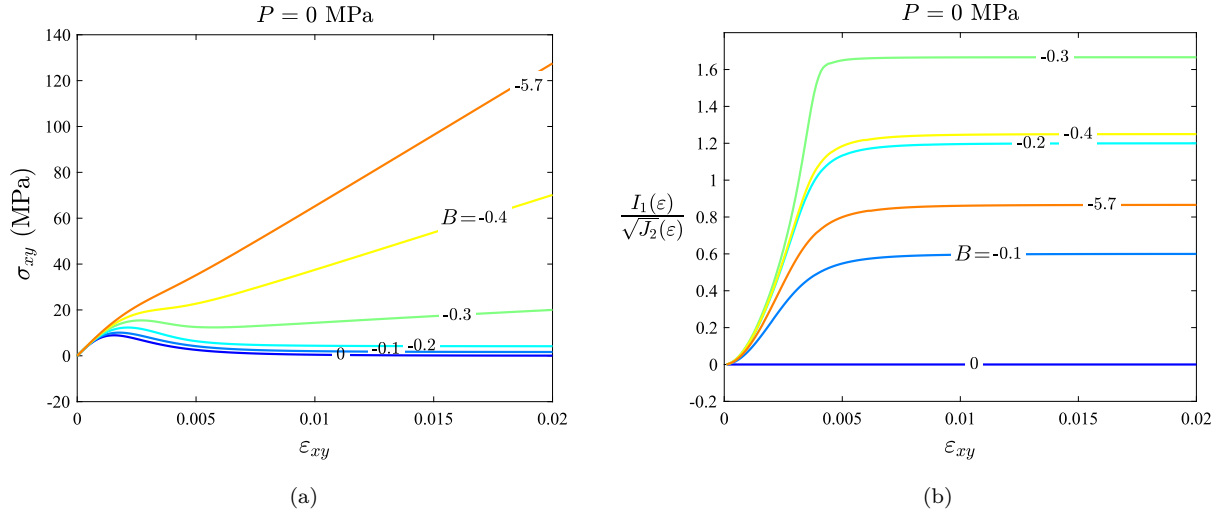


Figure 5: Single element under shear deformation. Results obtained without vertical pressure ($P = 0 \text{ MPa}$) for selected choices of B : (a) shear stress σ_{xy} versus shear strain ε_{xy} , and (b) $I_1(\boldsymbol{\varepsilon})/\sqrt{J_2(\boldsymbol{\varepsilon})}$ versus shear strain ε_{xy} .

Next, the influence of vertical pressure is examined. The results obtained for selected values of P and B are shown in Fig. 6. For the case of $B = 0$ (Fig. 6a), the shear stress shows a negligible sensitivity to the vertical pressure and no frictional effect (σ_{xy} drops to zero as $\phi \rightarrow 1$). The peak stress value shows some sensitivity to P due to the interplay between damage and the applied pressure. The results seen for $B = 0$ contrast with those obtained for non-zero B values (Figs. 6b-d). For $B \neq 0$, friction plays a noticeable role with the shear stress increasing with P . Also, the slope of the shear stress-strain curve increases with the absolute value of B .

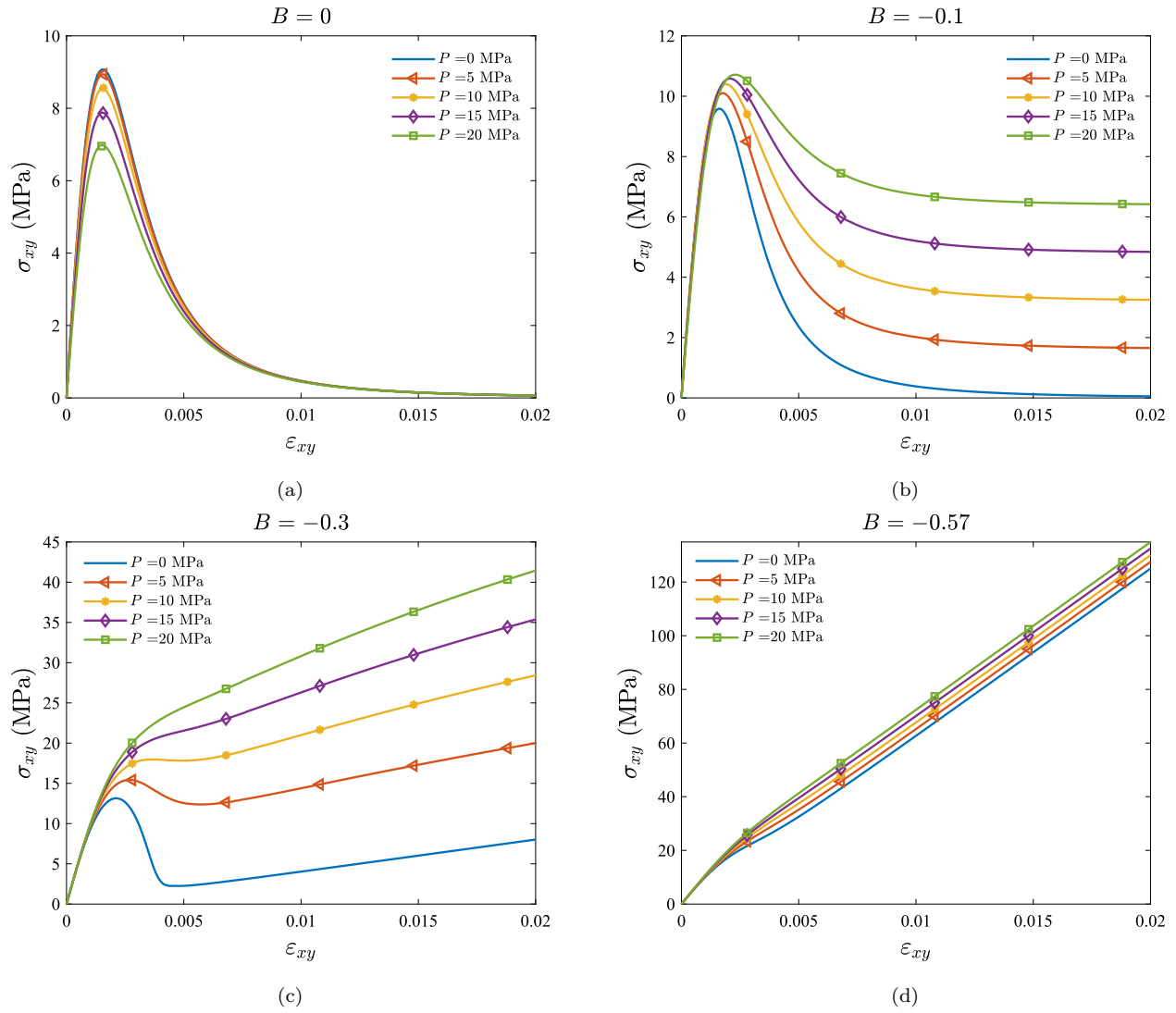


Figure 6: Single element under shear deformation. Shear stress versus shear strain predictions as a function of P for selected values of the B parameter: (a) $B = 0$, (b) $B = -0.1$, (c) $B = -0.3$, and (c) $B = -0.57$.

The ability of the Drucker-Prager based split model to capture the dilatancy effect is further explored by plotting the predictions of volumetric strain $\epsilon_{vol} = \epsilon_{xx} + \epsilon_{yy} + \epsilon_{zz}$ for selected values of the parameter B and the applied pressure P . As shown in Fig. 7, the volumetric strain ϵ_{vol} increases with the shear strain ϵ_{xy} in all cases except for that of $B = 0$. The effect of dilatancy is clear in all $B \neq 0$ calculations (Fig. 7b-d). In addition, the results show that higher pressures lead to reductions in volume as a result of material damage.

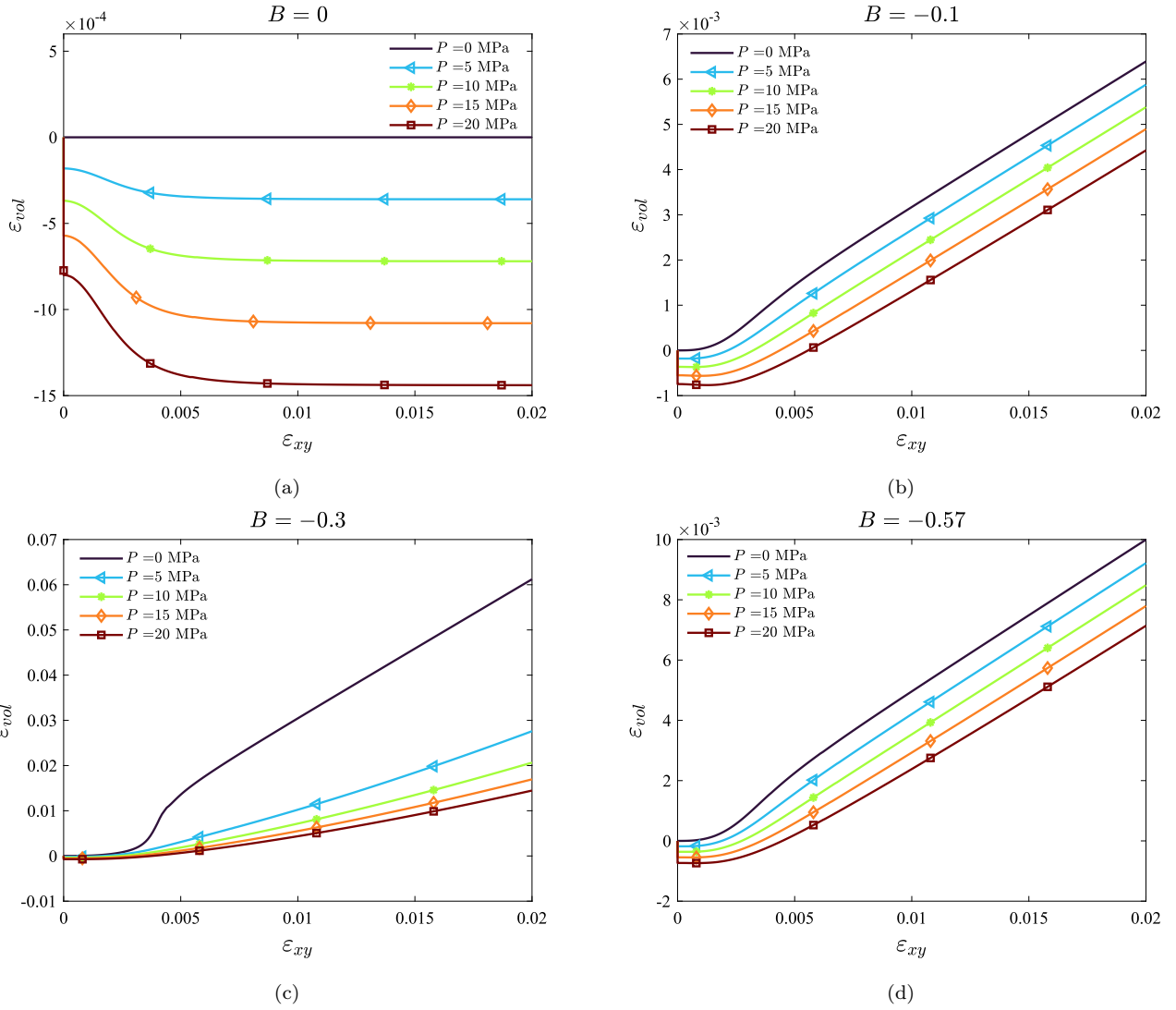


Figure 7: Single element under shear deformation. Volumetric strain versus shear strain predictions as a function of P for selected values of the B parameter: (a) $B = 0$, (b) $B = -0.1$, (c) $B = -0.3$, and (c) $B = -0.57$.

4.2. Virtual Direct Shear Tests (DST)

Next, the Direct Shear Test (DST) is simulated to evaluate the model behaviour in an experimental configuration that is widely used for finding the frictional parameters of soil and rock materials, such as cohesion and friction angle. The geometry and boundary conditions of the model are shown in Fig. 8. A vertical pressure P is applied at the top edge, followed by a horizontal displacement u_x over a 24 mm long region of the left edge. We consider three scenarios to assess the role of the vertical pressure: $P = 20$ MPa, $P = 10$ MPa and no pressure ($P = 0$). The elastic properties are taken as $E = 25$ GPa and $\nu = 0.2$, while the fracture parameters are given by $G_c = 0.15$ kJ/m² and $\ell = 0.2$ mm. The model is discretised with approximately 80,000 4-node plane strain quadrilateral elements with reduced integration. The mesh is refined along the expected crack propagation region,

such that the characteristic element size is at least half of the phase field length scale ℓ .

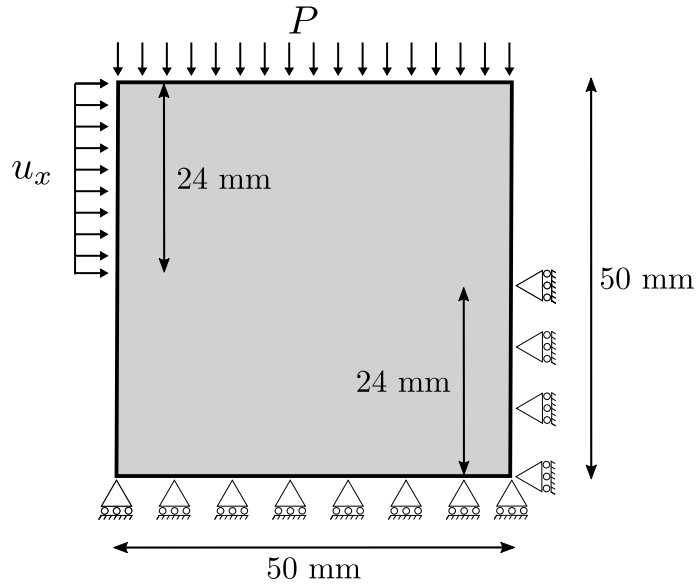


Figure 8: Direct shear test (DST) model. Geometry and boundary conditions.

The results obtained are shown in Fig. 9, in terms of the shear force versus the applied displacement u_x , and as a function of the applied pressure P . The case of no pressure shows a complete drop of the load carrying capacity as a result of damage, in agreement with experimental DST observations on geomaterials. However, a residual load is retained when a vertical pressure is applied, and this increases with the magnitude of P . Also, in all cases some oscillations can be seen in the force versus displacement response, which can be attributed to the effect of grain interlocking.

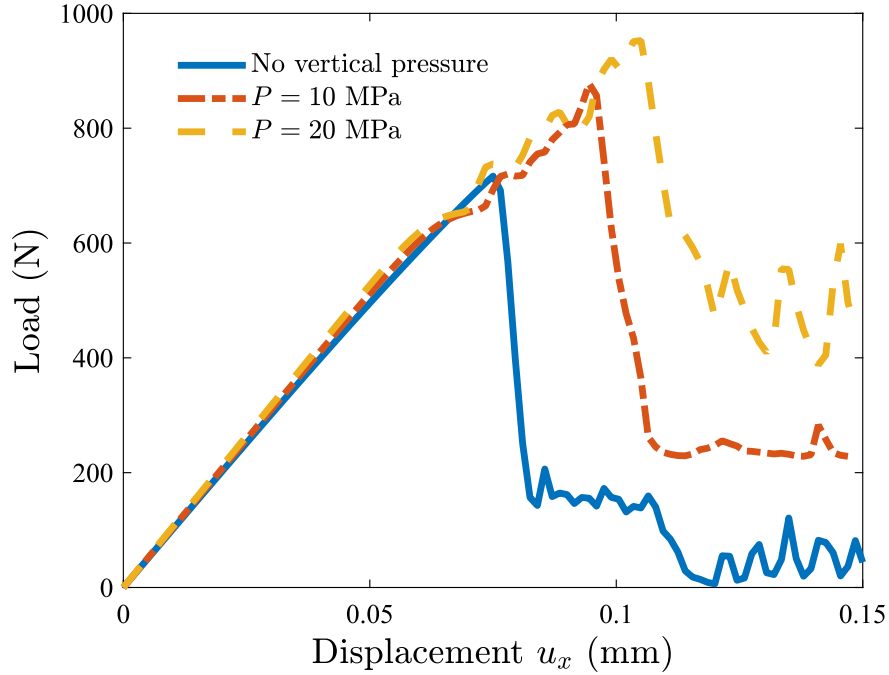


Figure 9: Direct shear test (DST). Shear load versus applied displacement results as a function of the applied pressure P .

Finally, the predicted crack trajectories are shown in Fig. 10, as a function of P , by plotting contours of the phase field order parameter ϕ . The results reveal an influence of the applied pressure on the cracking pattern. The lower the vertical pressure the more tortuous the crack path. Also, increasing the applied pressure leads to an accumulation of damage at the edges of the loading region, which are then connected through a crack that propagates across the sample.

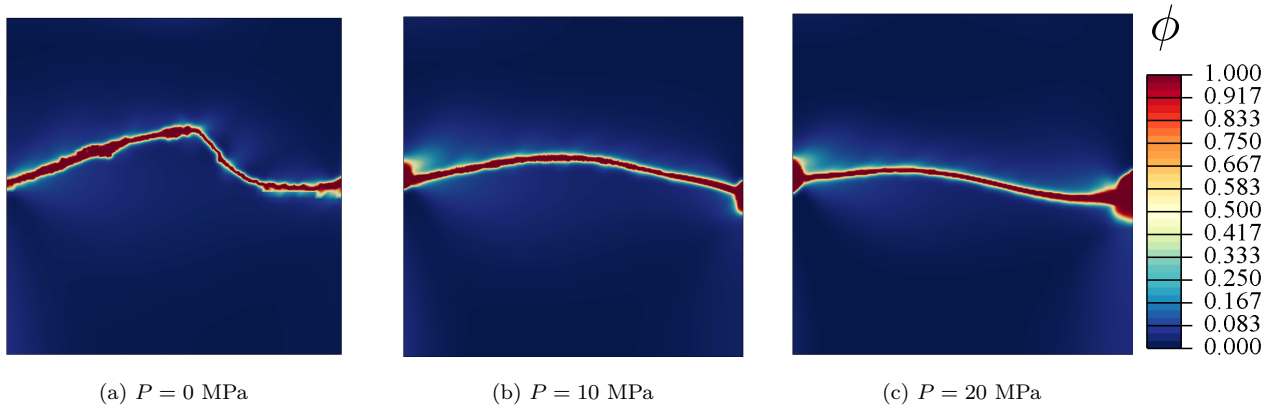


Figure 10: Direct shear test (DST). Predicted cracking patterns, as shown through contours of the phase field ϕ for selected values of the applied pressure: (a) $P = 0$, (b) $P = 10$ MPa, and (c) $P = 20$ MPa.

4.3. Uniaxial and triaxial compression testing of concrete

The third case study involves the failure of concrete samples undergoing uniaxial and triaxial compression. The aim is to investigate the abilities of the Drucker-Prager formulation presented to capture the effect of confinement. Mimicking the commonly used experimental setup, a cylindrical specimen is subjected to a compressive displacement at the top, while its surface is subjected to a confinement pressure. In the numerical model, we take advantage of axial symmetry and simulate a 2D section of the sample. The dimensions and loading configuration of the model are given in Fig. 11. To reproduce with fidelity the experimental conditions, we choose to simulate the contact between the jaws and the concrete sample. The jaws are assumed to be made of steel, with elastic properties $E = 210$ GPa and $\nu = 0.3$. The contact between the jaws and the disk is defined as a surface to surface contact with a finite sliding formulation. The tangential contact behaviour is assumed to be frictionless while the normal behaviour is based on a hard contact scheme, where the contact constraint is enforced with a Lagrange multiplier representing the contact pressure in a mixed formulation. The material properties of concrete are taken to be $E = 25$ GPa, $\nu = 0.2$, $\ell = 0.4$ mm, $G_c = 0.15$ kJ/m², and $B = -0.12$. Linear quadrilateral axisymmetric elements are used to discretise the model. In particular, approximately 35,000 elements are used to discretise the concrete sample while 1,500 elements are employed in each of the jaws. The characteristic element size in the areas of interest is below 0.2 mm, half of the phase field length scale. The ratio between the applied pressure and the prescribed displacement equals $P/u_y = 10$ MPa/mm.

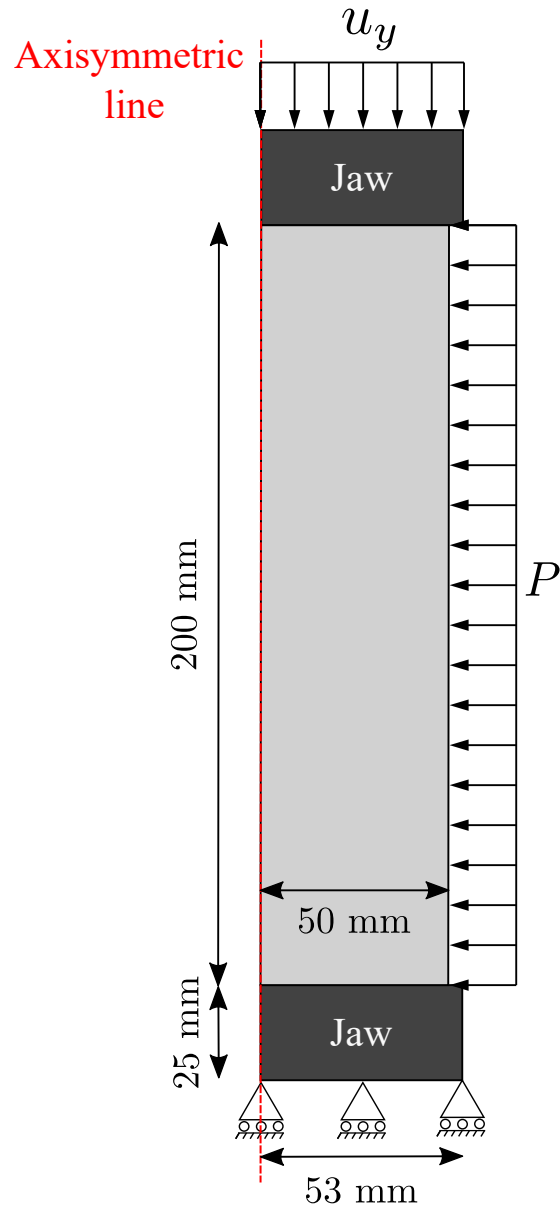


Figure 11: Compressive failure of concrete. Model geometry, dimensions and boundary conditions.

The force versus displacement responses predicted with and without a confinement pressure are shown in Fig. 12. It can be seen that, in agreement with expectations, the application of a confinement pressure increases the magnitude of the critical load. The ultimate strength of the sample with confinement is found to be almost 40% higher than the unconfined one. Also, a more brittle behaviour is observed in the unconfined sample, with a sharper drop in the load carrying capacity at the moment of failure.

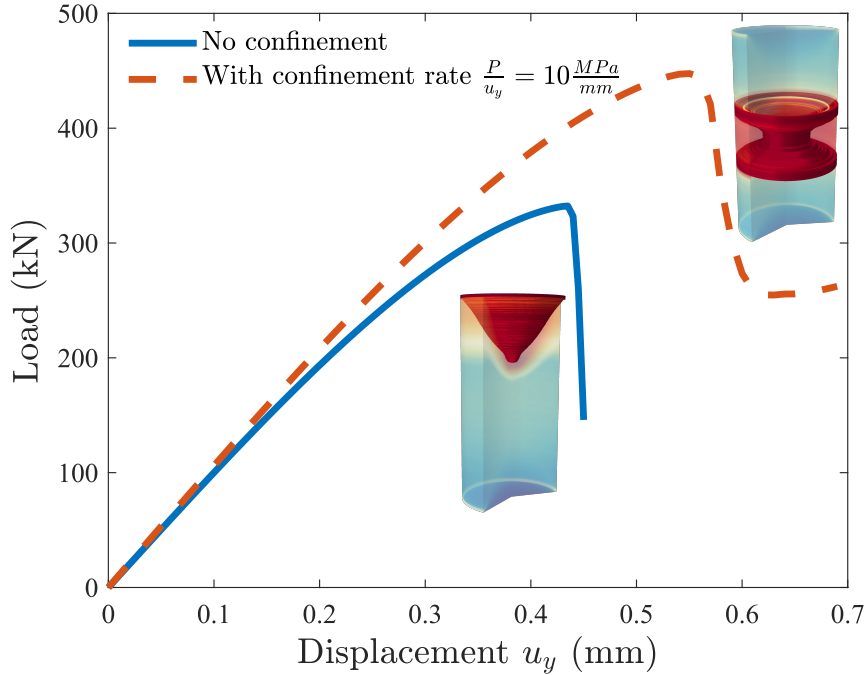


Figure 12: Compressive failure of concrete. Predicted load versus displacement curves for a sample without confinement pressure and one with a confinement pressure-prescribed displacement ratio of $P/u_y = 10$ MPa/mm.

Qualitative differences are found between the cracking patterns observed for the confined and unconfined experiments. As shown in Fig. 13, in the unconfined specimen the crack starts from the edge and propagates gradually towards the centre, creating a cone shape fracture. This is in agreement with the cracking patterns observed experimentally for brittle solids in the absence of confinement [38, 39]. However, in the confined specimen, see Fig. 14, the crack nucleates at the centre of the sample and then propagates towards the surface, exhibiting a double shear failure mode. Such a cracking pattern has also been reported in experiments conducted under confinement pressures [39]. Of interest for future work is the analysis of the influence of friction between the sample and the compression plates, which can be readily be incorporated into the present framework and has been argued to influence cracking patterns [28, 40].

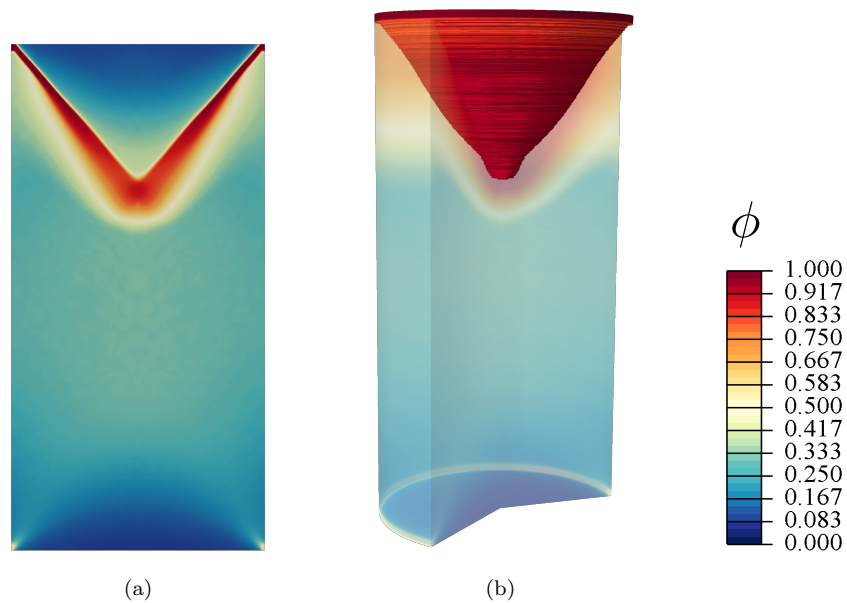


Figure 13: Compressive failure of concrete. Cracking patterns for the unconfined sample, as described by the phase field ϕ contours: (a) axisymmetric 2D results, and (b) 3D visualisation.

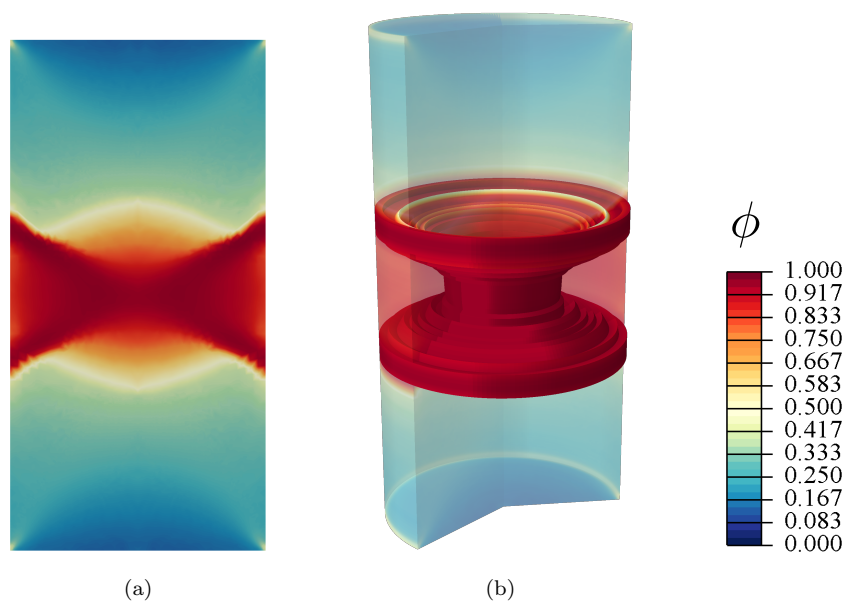


Figure 14: Compressive failure of concrete. Cracking patterns for the confined sample, as described by the phase field ϕ contours: (a) axisymmetric 2D results, and (b) 3D visualisation. The ratio between the applied pressure and the prescribed displacement equals $P/u_y = 10$ MPa/mm.

4.4. Localised failure of a soil slope

Finally, in our last case study, we compare the predictions of the Drucker-Prager strain energy decomposition formulation to those obtained with what are arguably the most widely use strain energy decompositions in the literature: the volumetric-deviatoric split by Amor *et al.* [25] and the

spectral decomposition by Miehe and co-workers [26]. First, the damaged and stored (elastic) strain energy densities are defined for these two approaches, following the terminology of Section 2. Thus, the volumetric-deviatoric split is characterised by,

$$\psi_d(\boldsymbol{\varepsilon}) = \frac{1}{2}K\langle\text{tr}(\boldsymbol{\varepsilon})\rangle_+^2 + \mu(\boldsymbol{\varepsilon}' : \boldsymbol{\varepsilon}') , \quad \psi_s(\boldsymbol{\varepsilon}) = \frac{1}{2}K\langle\text{tr}(\boldsymbol{\varepsilon})\rangle_-^2 . \quad (31)$$

Here, $\langle a \rangle_{\pm} = (a \pm |a|) / 2$, and $\boldsymbol{\varepsilon}' = \boldsymbol{\varepsilon} - \text{tr}(\boldsymbol{\varepsilon}) \mathbf{I} / 3$. While the strain energy decomposition by Miehe *et al.* [26] reads,

$$\psi_d(\boldsymbol{\varepsilon}) = \frac{1}{2}\lambda\langle\text{tr}(\boldsymbol{\varepsilon})\rangle_+^2 + \mu\text{tr}\left[\left(\boldsymbol{\varepsilon}^+\right)^2\right] , \quad \psi_s(\boldsymbol{\varepsilon}) = \frac{1}{2}\lambda\langle\text{tr}(\boldsymbol{\varepsilon})\rangle_-^2 + \mu\text{tr}\left[\left(\boldsymbol{\varepsilon}^-\right)^2\right] , \quad (32)$$

where a spectral decomposition is applied to the strain tensor, such that $\boldsymbol{\varepsilon}^{\pm} = \sum_{a=1}^3 \langle \varepsilon_I \rangle_{\pm} \mathbf{n}_I \otimes \mathbf{n}_I$, with ε_I and \mathbf{n}_I being, respectively, the strain principal strains and principal strain directions (with $I = 1, 2, 3$).

The boundary value problem under consideration is inspired by the work by Regueiro and Borja [41], where a strong discontinuity approach was used to predict the stability of a soil slope. This problem was also recently investigated by Fei and Choo [42] using a phase field-based frictional shear fracture model. The geometry, dimensions and boundary conditions are given in Fig. 15. A rigid foundation is placed at the crest of the slope, as shown in Fig. 15. First, a gravity load is applied, followed by a vertical displacement that is prescribed at the centre of the rigid foundation. The material properties of the soil are given by $E = 10$ MPa, $\nu = 0.4$, $\ell = 0.1$ m, $G_c = 0.2$ kJ/m², and $B = 0.12$. Approximately 50,000 quadrilateral linear elements are used, with the mesh being refined in the crack propagation region through an iterative process. In all cases, the characteristic size of the elements in the damaged region is five times smaller than the phase field length scale ℓ .

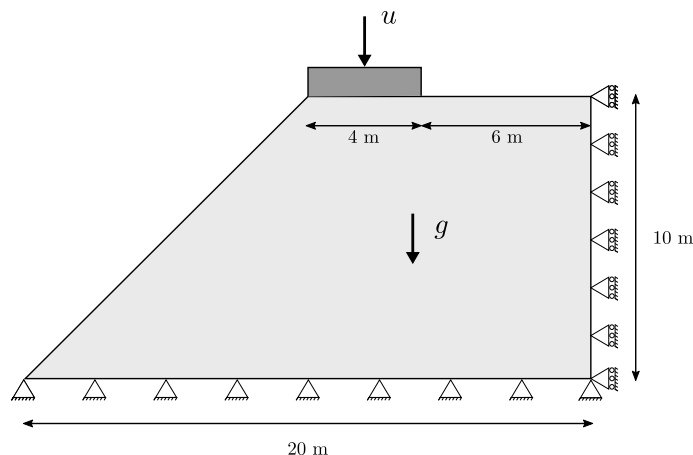


Figure 15: Localised failure of a soil slope. Geometry and boundary conditions.

The results obtained are given in Fig. 16. The cracking patterns are shown for each of the three strain energy decompositions considered, by means of contours of the phase field order parameter ϕ . As shown in Fig. 16a, the volumetric-deviatoric split by Amor *et al.* [25] predicts a localised failure under the rigid foundation. The spectral decomposition by Miehe and co-workers [26] is also unable to adequately capture the localised failure of the soil slope. As shown in Fig. 16b, damage accumulates under the rigid foundation, showing a V-type of failure. On the other hand, the Drucker-Prager formulation presented in Section 3 is able to appropriately simulate the localised failure of the soil slope. Cracking initiates from the right corner of the foundation and propagates towards the edge of the slope, in a very similar pattern to that reported by other numerical experiments [41, 42].

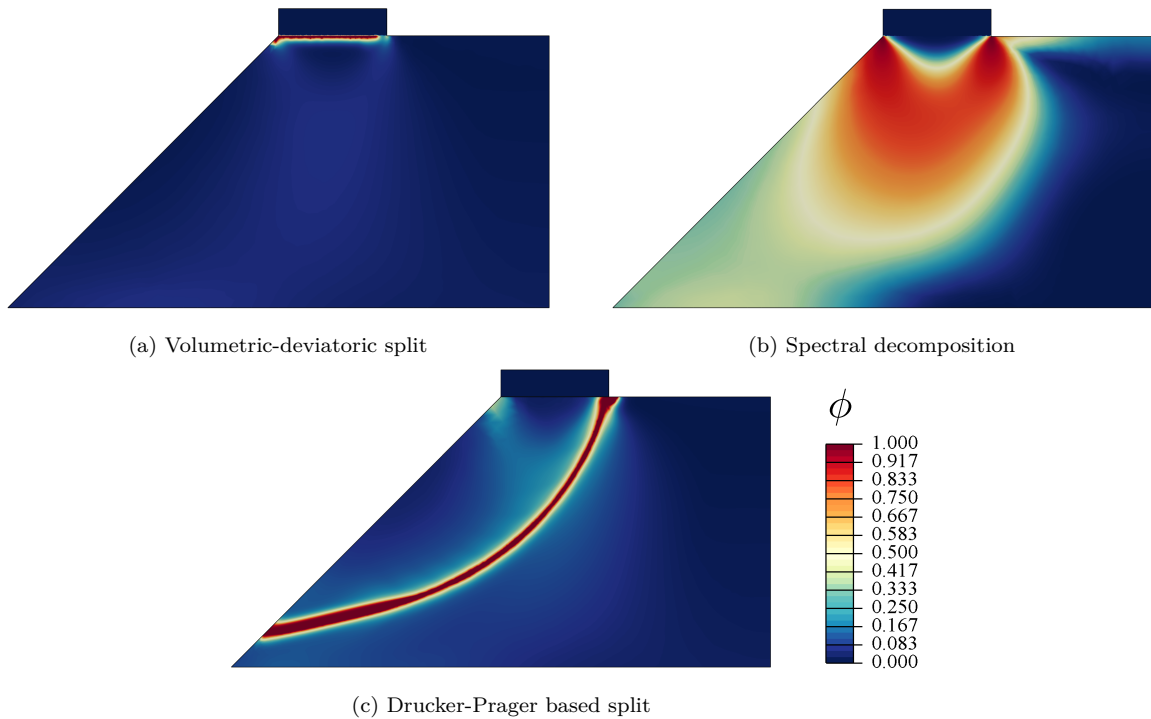


Figure 16: Localised failure of a soil slope. Failure patterns as described by the contours of the phase field order parameter for: (a) the volumetric-deviatoric split, Eq. (31), (b) the spectral decomposition, Eq. (32), and (c) the Drucker-Prager based split presented, Eqs. (27)-(28).

5. Discussion

The aim of the present work is to present a general approach to decompose the phase field fracture driving force, the strain energy density, so as to encompass any arbitrary choice of failure criteria. One important motivation for this work lies in the need to enrich the phase field fracture method to go beyond its assumed symmetric tension-compression fracture behaviour to adequately predict crack nucleation and growth in multi-axial stress states. The potential of the general methodology

presented is demonstrating by particularising it to the Drucker-Prager failure surface. In doing so, we establish a connection with the recent work by De Lorenzis and Maurini [33]. De Lorenzis and Maurini [33] showed analytically that phase field fracture can be generalised to accommodate arbitrary multiaxial failure surfaces and thus faithfully predict crack nucleation without the need to recur to non-variational models. They also chose to particularise their approach to a Drucker-Prager failure surface. Thus, both works reach the same theoretical outcome from different angles. Since our paper also includes a numerical implementation, it complements and extends the work by De Lorenzis and Maurini [33], confirming their findings. It is also worth noting that our analysis is not limited to nucleation but also considers the propagation of cracks until failure. To achieve this, it is here assumed that the same surface in the multiaxial stress space characterises the limit of the elastic domain ($\phi > 0$) and the fully damaged state ($\phi = 1$). Several numerical experiments are reported to showcase the ability of the model to predict crack nucleation and growth in boundary value problems exhibiting multi-axial loading and mixed-mode fracture conditions. An alternative approach is that proposed by Kumar *et al.* [43], where an external driving force is defined to recover a Drucker-Prager failure surface. However, this comes at the cost of losing the variational consistency.

6. Conclusions

We have presented a general framework for determining the strain energy decomposition associated with arbitrary choices of constitutive behaviour and failure criterion. This is of importance for phase field fracture modelling as it opens a new avenue for incorporating multi-axial failure surfaces and thus appropriately capturing crack nucleation in a wide range of materials. In particular, this is needed to predict the compressive failure of brittle and quasi-brittle solids such as concrete and geomaterials. Accordingly, we chose to illustrate our framework by particularising it to the case of a Drucker-Prager failure surface. We numerically implemented the resulting formulation for the strain energy decomposition and used it to simulate fracture phenomena in brittle materials. Specifically, the potential of the Drucker-Prager based formulation presented was showcased by addressing four paradigmatic case studies. The behaviour of a single element undergoing shear deformations and vertical pressure was investigated first. The results showed that the model is capable of capturing the role of friction and dilatancy. The magnitude of the shear stresses attained was highest for higher values of the pressure and of Drucker-Prager’s parameter B . Direct Shear Tests (DST) were subsequently simulated showing a noticeable influence of the applied pressure. The lower the pressure, the more tortuous the crack path and the lower the magnitude of the residual load predicted.

Thirdly, the failure of cylindrical samples under uniaxial and triaxial compression was investigated. The results revealed a qualitative impact of the confinement pressure on both the cracking patterns and the force versus displacement response predicted. Cracking predictions appear to agree with experimental observations, shifting from a cone shape fracture to a double shear failure mode with increasing confinement. Finally, we simulated the localised failure of a soil slope using three different strain energy splits: our Drucker-Prager approach and the widely used volumetric-deviatoric [25] and spectral [26] decompositions. The results show that only the Drucker-Prager based formulation is able to adequately predict the fracture behaviour. Accordingly, the present work: (i) opens a new avenue for incorporating multi-axial failure criteria in phase field fracture modelling, and (ii) demonstrates the potential of Drucker-Prager based phase field formulations for predicting compressive failures in materials exhibiting asymmetric tension-compression fracture behaviour.

7. Acknowledgments

The authors acknowledge financial support from the Ministry of Science, Innovation and Universities of Spain through grant PGC2018-099695-B-I00. E. Martínez-Pañeda was supported by an UKRI Future Leaders Fellowship (grant MR/V024124/1).

Appendix A. The relation of stress and strain invariants

In the following, we shall show how Eq. (14) can be derived for any choice of strain energy density in the form of $\psi(I_1(\boldsymbol{\varepsilon}), J_2(\boldsymbol{\varepsilon}))$. First, let us express the Cauchy stress as:

$$\boldsymbol{\sigma}(\boldsymbol{\varepsilon}) = \frac{\partial\psi(I_1(\boldsymbol{\varepsilon}), J_2(\boldsymbol{\varepsilon}))}{\partial\boldsymbol{\varepsilon}} = \frac{\partial\psi(I_1(\boldsymbol{\varepsilon}), J_2(\boldsymbol{\varepsilon}))}{\partial I_1(\boldsymbol{\varepsilon})} \frac{\partial I_1(\boldsymbol{\varepsilon})}{\partial\boldsymbol{\varepsilon}} + \frac{\partial\psi(I_1(\boldsymbol{\varepsilon}), J_2(\boldsymbol{\varepsilon}))}{\partial J_2(\boldsymbol{\varepsilon})} \frac{\partial J_2(\boldsymbol{\varepsilon})}{\partial\boldsymbol{\varepsilon}}. \quad (\text{A.1})$$

The variations of the first two invariants of the strain tensor are written as,

$$\frac{\partial I_1(\boldsymbol{\varepsilon})}{\partial\boldsymbol{\varepsilon}} = \mathbf{I}, \quad \frac{\partial J_2(\boldsymbol{\varepsilon})}{\partial\boldsymbol{\varepsilon}} = \boldsymbol{\varepsilon}' \quad (\text{A.2})$$

where \mathbf{I} denotes the identity tensor and $\boldsymbol{\varepsilon}'$ is the deviatoric part of strain tensor. On the other side, the first invariant of the Cauchy stress tensor is given by

$$I_1(\boldsymbol{\sigma}) = \text{tr}(\boldsymbol{\sigma}) = \text{tr} \left(\frac{\partial\psi(I_1(\boldsymbol{\varepsilon}), J_2(\boldsymbol{\varepsilon}))}{\partial\boldsymbol{\varepsilon}} \right) = \frac{\partial\psi(I_1(\boldsymbol{\varepsilon}), J_2(\boldsymbol{\varepsilon}))}{\partial I_1(\boldsymbol{\varepsilon})} \text{tr} \left(\frac{\partial I_1(\boldsymbol{\varepsilon})}{\partial\boldsymbol{\varepsilon}} \right) + \frac{\partial\psi(I_1(\boldsymbol{\varepsilon}), J_2(\boldsymbol{\varepsilon}))}{\partial J_2(\boldsymbol{\varepsilon})} \text{tr} \left(\frac{\partial J_2(\boldsymbol{\varepsilon})}{\partial\boldsymbol{\varepsilon}} \right) \quad (\text{A.3})$$

Eq. (A.3) can be simplified by considering $\text{tr}(\partial I_1(\boldsymbol{\varepsilon})/\partial\boldsymbol{\varepsilon}) = 3$ and $\text{tr}(\partial J_2(\boldsymbol{\varepsilon})/\partial\boldsymbol{\varepsilon}) = 0$, such that

$$I_1(\boldsymbol{\sigma}) = 3 \frac{\partial\psi(I_1(\boldsymbol{\varepsilon}), J_2(\boldsymbol{\varepsilon}))}{\partial I_1(\boldsymbol{\varepsilon})}. \quad (\text{A.4})$$

which corresponds to Eq. (14)a, the equation relating the first invariant of stress $I_1(\boldsymbol{\sigma})$ with the first invariant of strain $I_1(\boldsymbol{\varepsilon})$. Next, we use Eqs. (A.1) and (A.4) to formulate the deviatoric part of the Cauchy stress tensor $\boldsymbol{\sigma}'$ as

$$\boldsymbol{\sigma}' = \boldsymbol{\sigma} - \frac{1}{3} \text{tr}(\boldsymbol{\sigma}) \mathbf{I} = \boldsymbol{\varepsilon}' \frac{\partial \psi(I_1(\boldsymbol{\varepsilon}), J_2(\boldsymbol{\varepsilon}))}{\partial J_2(\boldsymbol{\varepsilon})}. \quad (\text{A.5})$$

Then, Eq. (14)b, relating the second stress invariant $J_2(\boldsymbol{\sigma})$ with its strain-based counterpart $J_2(\boldsymbol{\varepsilon})$ can be obtained by substituting Eq. (A.5) into the definition of $J_2(\boldsymbol{\sigma})$, rendering

$$J_2(\boldsymbol{\sigma}) = \frac{1}{2} \text{tr}((\boldsymbol{\sigma}')^2) = \frac{1}{2} \text{tr}((\boldsymbol{\varepsilon}')^2) \left(\frac{\partial \psi(I_1(\boldsymbol{\varepsilon}), J_2(\boldsymbol{\varepsilon}))}{\partial J_2(\boldsymbol{\varepsilon})} \right)^2 = J_2(\boldsymbol{\varepsilon}) \left(\frac{\partial \psi(I_1(\boldsymbol{\varepsilon}), J_2(\boldsymbol{\varepsilon}))}{\partial J_2(\boldsymbol{\varepsilon})} \right)^2. \quad (\text{A.6})$$

Appendix B. Strain-based mapping of the stress state scenarios

Any relevant stress state can be classified as one of three potential scenarios in the $(I_1(\boldsymbol{\sigma}), \sqrt{J_2(\boldsymbol{\sigma})})$ stress space. However, for numerical reasons, the stored (reversible) ψ_s and damaged ψ_d strain energy densities are formulated in terms of the strain tensor $\boldsymbol{\varepsilon}$, see Eqs. (27)-(28). Thus, for completeness, we proceed to describe the derivation of Eqs. (27)-(28) for the stress scenarios discussed in Section 3.

Consider first the third regime, given by Eqs. (27)c and (28)c, where $I_1(\boldsymbol{\sigma}) < 0$ and the stress state is below the failure envelope. Under these conditions, damage does not evolve and consequently the stored part of the strain energy density equals the total one $\psi_s(\boldsymbol{\varepsilon}) = \psi_0(\boldsymbol{\varepsilon})$. Specifically, the stress state in this regime fulfills the following:

$$\sqrt{J_2(\boldsymbol{\sigma})} < BI_1(\boldsymbol{\sigma}) \quad \text{and} \quad I_1(\boldsymbol{\sigma}) \leq 0. \quad (\text{B.1})$$

Where the stress invariants can be written as,

$$\begin{aligned} I_1(\boldsymbol{\sigma}) &= 3 \frac{\partial \psi(\boldsymbol{\varepsilon})}{\partial I_1(\boldsymbol{\varepsilon})} = 3g(\phi) \frac{\partial \psi_0(\boldsymbol{\varepsilon})}{\partial I_1(\boldsymbol{\varepsilon})} + 3(1-g(\phi)) \frac{\partial \psi_s(\boldsymbol{\varepsilon})}{\partial I_1(\boldsymbol{\varepsilon})}, \\ J_2(\boldsymbol{\sigma}) &= J_2(\boldsymbol{\varepsilon}) \left(\frac{\partial \psi(\boldsymbol{\varepsilon})}{\partial J_2(\boldsymbol{\varepsilon})} \right)^2 = g(\phi) J_2(\boldsymbol{\varepsilon}) \left(\frac{\partial \psi_0(\boldsymbol{\varepsilon})}{\partial J_2(\boldsymbol{\varepsilon})} \right)^2 + (1-g(\phi)) J_2(\boldsymbol{\varepsilon}) \left(\frac{\partial \psi_s(\boldsymbol{\varepsilon})}{\partial J_2(\boldsymbol{\varepsilon})} \right)^2. \end{aligned} \quad (\text{B.2})$$

Considering that, in this scenario, $\psi_s(\boldsymbol{\varepsilon}) \equiv \psi_0(\boldsymbol{\varepsilon})$ and inserting Eq. (B.2) into the first condition of Eq. (B.1), one reaches

$$\sqrt{J_2(\boldsymbol{\varepsilon})} \frac{\partial \psi_0(\boldsymbol{\varepsilon})}{\partial J_2(\boldsymbol{\varepsilon})} < 3B \frac{\partial \psi_0(\boldsymbol{\varepsilon})}{\partial I_1(\boldsymbol{\varepsilon})} \quad (\text{B.3})$$

Now, recalling the definition of ψ_0 , Eq. (13), Eq. (B.3) can be re-formulated as

$$2\mu \sqrt{J_2(\boldsymbol{\varepsilon})} < 3BK I_1(\boldsymbol{\varepsilon}) \quad (\text{B.4})$$

On the other side, the second condition of Eq. (B.1) can be described as a function of the strain tensor as follows,

$$3\frac{\partial\psi_0(\boldsymbol{\varepsilon})}{\partial I_1(\boldsymbol{\varepsilon})} \leq 0 \quad (\text{B.5})$$

Implying that $I_1(\boldsymbol{\varepsilon}) \leq 0$. However, this has already been satisfied by Eq. (B.4) as $\sqrt{J_2(\boldsymbol{\varepsilon})}$ is a positive value and the parameter B is always zero or negative, such that $I_1(\boldsymbol{\varepsilon})$ must be negative to satisfy Eq. (B.3).

The second regime in the $(I_1(\boldsymbol{\sigma}), \sqrt{J_2(\boldsymbol{\sigma})})$ stress space corresponds to that where $I_1(\boldsymbol{\sigma}) \leq 0$ and the stress state is above the failure criterion; i.e.,

$$\sqrt{J_2(\boldsymbol{\sigma})} \geq BI_1(\boldsymbol{\sigma}) \quad \text{and} \quad I_1(\boldsymbol{\sigma}) \leq 0. \quad (\text{B.6})$$

Given that Eq. (B.3) provides the strain condition for the case where the stress state is below the failure criterion, it follows that the relevant condition for the second regime where the stress state is above the failure criterion is given by

$$2\mu\sqrt{J_2(\boldsymbol{\varepsilon})} \geq 3BI_1(\boldsymbol{\varepsilon}) \quad (\text{B.7})$$

Then, the second condition in Eq. (B.6) can be expressed as:

$$g(\phi)KI_1(\boldsymbol{\varepsilon}) + \frac{K\mu}{9B^2K + \mu}(1 - g(\phi)) \left(I_1(\boldsymbol{\varepsilon}) + 6B\sqrt{J_2(\boldsymbol{\varepsilon})} \right) \leq 0. \quad (\text{B.8})$$

Which, considering that $g(\phi = 1) = 0$, can be reduced to,

$$I_1(\boldsymbol{\varepsilon}) \leq -6B\sqrt{J_2(\boldsymbol{\varepsilon})} \quad (\text{B.9})$$

Accordingly, the conditions for the second regime, in terms of the strain tensor, are given by (B.7) and (B.9).

The remaining conditions are applicable for the first regime in the stress space, where $I_1(\boldsymbol{\sigma})$ is positive:

$$\mu\sqrt{J_2(\boldsymbol{\varepsilon})} \geq 3BK I_1(\boldsymbol{\varepsilon}); \quad -6B\sqrt{J_2(\boldsymbol{\varepsilon})} < I_1(\boldsymbol{\varepsilon}), \quad (\text{B.10})$$

where the first condition can be neglected as it is satisfied by the second one.

Appendix C. Additional details of the finite element implementation

Appendix C.1. Strong and weak formulations

Considering Eq. (2) and the constitutive choices in Eq. (3), Griffith's regularised energy functional can be formulated as,

$$\mathcal{E}_\ell = \int_{\Omega} \psi_s(\boldsymbol{\varepsilon}(\mathbf{u})) + (1 - \phi)^2 \psi_d(\boldsymbol{\varepsilon}(\mathbf{u})) \, dV + \int_V G_c \left(\frac{1}{2\ell} \phi^2 + \frac{\ell}{2} |\nabla \phi|^2 \right) \, dV \quad (\text{C.1})$$

The stationary of \mathcal{E}_ℓ with respect to the primal kinematic variables renders,

$$\partial \mathcal{E}_\ell = \int_{\Omega} \left\{ \left[(1 - \phi)^2 \frac{\partial \psi_d(\boldsymbol{\varepsilon})}{\partial \boldsymbol{\varepsilon}} + \frac{\partial \psi_s(\boldsymbol{\varepsilon})}{\partial \boldsymbol{\varepsilon}} \right] \delta \boldsymbol{\varepsilon} - 2(1 - \phi) \delta \phi \psi_d(\boldsymbol{\varepsilon}) + G_c \left[\frac{1}{\ell} \phi \delta \phi + \ell \nabla \phi \cdot \nabla \delta \phi \right] \right\} \, dV \quad (\text{C.2})$$

Accordingly, the strong form can be readily derived by considering the variation in the external work,

$$\delta W_{ext} = \int_{\Omega} \mathbf{b} \cdot \delta \mathbf{u} \, dV + \int_{\partial \Omega_h} \mathbf{h} \cdot \delta \mathbf{u} \, dA \quad (\text{C.3})$$

enforcing equilibrium of the external and internal virtual works,

$$\partial \mathcal{E}_\ell - \delta W_{ext} = 0 \quad (\text{C.4})$$

and making use of Gauss' divergence theorem,

$$\begin{aligned} \nabla \cdot \left[(1 - \phi)^2 \frac{\partial \psi_d(\boldsymbol{\varepsilon})}{\partial \boldsymbol{\varepsilon}} + \frac{\partial \psi_s(\boldsymbol{\varepsilon})}{\partial \boldsymbol{\varepsilon}} \right] + \mathbf{b} &= \mathbf{0} \quad \text{in } \Omega \\ G_c \left(\frac{\phi}{\ell} - \ell \nabla^2 \phi \right) - 2(1 - \phi) \psi_d &= 0 \quad \text{in } \Omega \end{aligned} \quad (\text{C.5})$$

Appendix C.2. Heat transfer analogy

As discussed in Refs. [36, 37], we exploit the analogy with heat transfer to facilitate the numerical implementation of the phase field evolution equation. In the presence of a heat source r , the steady state equation for heat transfer has the following form,

$$k \nabla^2 T = -r \quad (\text{C.6})$$

where T is the temperature, and k is the thermal conductivity. Eq. (C.6) is analogous to the phase field evolution equation (C.5b) upon assuming $T \equiv \phi$, $k = 1$, and defining the heat source r as follows:

$$r = \frac{2(1 - \phi)\mathcal{H}}{\ell G_c} - \frac{\phi}{\ell^2} \quad (\text{C.7})$$

where, as discussed in Section 3, $\mathcal{H} = \max \psi_d(t)$ is a history field introduced to enforce damage irreversibility. Finally, the variation of the heat source with respect to the phase field (temperature) is derived as,

$$\frac{\partial r}{\partial \phi} = -\frac{2\mathcal{H}}{\ell G_c} - \frac{1}{\ell^2} \quad (\text{C.8})$$

Appendix C.3. Finite element discretisation

By exploiting the heat transfer analogy, one can implement the phase field formulation described in this paper into the finite element package **ABAQUS** using only a user material subroutine (**UMAT**). I.e., there is no need to explicitly define and implement the element stiffness matrix \mathbf{K}^e and the element residual vector \mathbf{R}^e . However, these are derived here for completeness. Consider the equilibrium of the external and internal virtual works presented in Section Appendix C.1. Decoupling the displacement and phase field problems, the weak form equations read,

$$\int_{\Omega} \left\{ \left[(1 - \phi)^2 \frac{\partial \psi_d(\boldsymbol{\varepsilon})}{\partial \boldsymbol{\varepsilon}} + \frac{\partial \psi_s(\boldsymbol{\varepsilon})}{\partial \boldsymbol{\varepsilon}} \right] : \delta \boldsymbol{\varepsilon} - \mathbf{b} \cdot \delta \mathbf{u} \right\} dV - \int_{\partial \Omega_h} \mathbf{h} \cdot \delta \mathbf{u} dA = 0. \quad (\text{C.9})$$

$$\int_{\Omega} \left\{ -2(1 - \phi) \delta \phi \mathcal{H} + G_c \left[\frac{1}{\ell} \phi \delta \phi + \ell \nabla \phi \nabla \delta \phi \right] \right\} dV = 0. \quad (\text{C.10})$$

Now, consider the following finite element discretisation. Adopting Voigt notation, the nodal variables for the displacement field $\hat{\mathbf{u}}$, and the phase field $\hat{\phi}$ are interpolated as:

$$\mathbf{u} = \sum_{i=1}^m \mathbf{N}_i \hat{\mathbf{u}}_i, \quad \phi = \sum_{i=1}^m N_i \hat{\phi}_i, \quad (\text{C.11})$$

where N_i is the shape function associated with node i and \mathbf{N}_i is the shape function matrix, a diagonal matrix with N_i in the diagonal terms. Also, m is the total number of nodes per element and $\hat{\mathbf{u}}_i$ and $\hat{\phi}_i$ respectively denote the displacement and phase field at node i . In a similar manner, the associated gradient quantities can be discretised using the corresponding \mathbf{B} -matrices, containing the derivative of the shape functions, such that:

$$\boldsymbol{\varepsilon} = \sum_{i=1}^m \mathbf{B}_i^u \hat{\mathbf{u}}_i, \quad \nabla \phi = \sum_{i=1}^m \mathbf{B}_i^\phi \hat{\phi}_i. \quad (\text{C.12})$$

The discretised residuals for each primal kinematic variable are then given by:

$$\mathbf{R}_i^u = \int_{\Omega} \left\{ (1 - \phi)^2 (\mathbf{B}_i^u)^T \frac{\partial \psi_d(\boldsymbol{\varepsilon})}{\partial \boldsymbol{\varepsilon}} + (\mathbf{B}_i^u)^T \frac{\partial \psi_s(\boldsymbol{\varepsilon})}{\partial \boldsymbol{\varepsilon}} \right\} dV - \int_{\Omega} (\mathbf{N}_i^u)^T \mathbf{b} dV - \int_{\partial \Omega_h} (\mathbf{N}_i^u)^T \mathbf{h} dA, \quad (\text{C.13})$$

$$\mathbf{R}_i^\phi = \int_{\Omega} \left\{ -2(1 - \phi) N_i \mathcal{H} + G_c \left[\frac{1}{\ell} N_i \phi + \ell (\mathbf{B}_i^\phi)^T \nabla \phi \right] \right\} dV \quad (\text{C.14})$$

And the consistent tangent stiffness matrices \mathbf{K} are obtained by differentiating the residuals with respect to the incremental nodal variables:

$$\mathbf{K}_{ij}^u = \frac{\partial \mathbf{R}_i^u}{\partial \mathbf{u}_j} = \int_{\Omega} \left\{ (1 - \phi)^2 (\mathbf{B}_i^u)^T \mathbf{C}_d \mathbf{B}_j^u + (\mathbf{B}_i^u)^T \mathbf{C}_s \mathbf{B}_j^u \right\} dV, \quad (\text{C.15})$$

$$\mathbf{K}_{ij}^{\phi} = \frac{\partial R_i^{\phi}}{\partial \phi_j} = \int_{\Omega} \left\{ \left(2\mathcal{H} + \frac{G_c}{\ell} \right) N_i N_j + G_{cl} \mathbf{B}_i^T \mathbf{B}_j \right\} dV, \quad (\text{C.16})$$

Here, the material jacobian \mathbf{C}_s can be defined as:

$$\mathbf{C}_s = \frac{\partial \psi_s}{\partial \boldsymbol{\varepsilon} \partial \boldsymbol{\varepsilon}} = \begin{cases} 0 & \text{for } -6B\sqrt{J_2(\boldsymbol{\varepsilon})} < I_1(\boldsymbol{\varepsilon}) \\ \mathbf{C}_s^{DP} & \text{for } -6B\sqrt{J_2(\boldsymbol{\varepsilon})} \geq I_1(\boldsymbol{\varepsilon}) \ \& \ 2\mu\sqrt{J_2(\boldsymbol{\varepsilon})} \geq 3BK I_1(\boldsymbol{\varepsilon}) \\ \mathbf{C}_0 & \text{for } 2\mu\sqrt{J_2(\boldsymbol{\varepsilon})} < 3BK I_1(\boldsymbol{\varepsilon}) \end{cases} \quad (\text{C.17})$$

where \mathbf{C}_0 is undamaged elastic tangent stiffness and \mathbf{C}_s^{DP} can be written as:

$$\begin{aligned} (C_s^{DP})_{ijkl} = & \frac{K\mu}{9B^2K + \mu} \left(\frac{\partial I_1}{\partial \varepsilon_{ij}} + \frac{3B}{\sqrt{J_2}} \frac{\partial J_2}{\partial \varepsilon_{ij}} \right) \left(\frac{\partial I_1}{\partial \varepsilon_{kl}} + \frac{3B}{\sqrt{J_2}} \frac{\partial J_2}{\partial \varepsilon_{kl}} \right) + \\ & \left(\frac{6Ba_1 (I_1 + 6B\sqrt{J_2})}{\sqrt{J_2}} \right) \left(\frac{\partial^2 J_2}{\partial \varepsilon_{ij} \partial \varepsilon_{kl}} - \frac{1}{2J_2} \frac{\partial J_2}{\partial \varepsilon_{ij}} \frac{\partial J_2}{\partial \varepsilon_{kl}} \right) \end{aligned} \quad (\text{C.18})$$

Finally, \mathbf{C}_d is obtained by exploiting the fact that $\psi_d = \psi_0 - \psi_s$:

$$\mathbf{C}_d = \frac{\partial \psi_d}{\partial \boldsymbol{\varepsilon} \partial \boldsymbol{\varepsilon}} = \frac{\partial \psi_0}{\partial \boldsymbol{\varepsilon} \partial \boldsymbol{\varepsilon}} - \frac{\partial \psi_s}{\partial \boldsymbol{\varepsilon} \partial \boldsymbol{\varepsilon}} = \mathbf{C}_0 - \mathbf{C}_s \quad (\text{C.19})$$

References

- [1] B. Bourdin, G. A. Francfort, J. J. Marigo, The variational approach to fracture, Springer Netherlands, 2008.
- [2] A. J. Pons, A. Karma, Helical crack-front instability in mixed-mode fracture, Nature 464 (7285) (2010) 85–89.
- [3] M. J. Borden, C. V. Verhoosel, M. A. Scott, T. J. R. Hughes, C. M. Landis, A phase-field description of dynamic brittle fracture, Computer Methods in Applied Mechanics and Engineering 217-220 (2012) 77–95.
- [4] P. K. Kristensen, E. Martínez-Pañeda, Phase field fracture modelling using quasi-Newton methods and a new adaptive step scheme, Theoretical and Applied Fracture Mechanics 107 (2020) 102446.

- [5] M. J. Borden, T. J. R. Hughes, C. M. Landis, A. Anvari, I. J. Lee, A phase-field formulation for fracture in ductile materials: Finite deformation balance law derivation, plastic degradation, and stress triaxiality effects, *Computer Methods in Applied Mechanics and Engineering* 312 (2016) 130–166.
- [6] S. S. Shishvan, S. Assadpour-asl, E. Martínez-Pañeda, A mechanism-based gradient damage model for metallic fracture, *Engineering Fracture Mechanics* 255 (2021) 107927.
- [7] Hirshikesh, S. Natarajan, R. K. Annabattula, E. Martínez-Pañeda, Phase field modelling of crack propagation in functionally graded materials, *Composites Part B: Engineering* 169 (2019) 239–248.
- [8] A. Quintanas-Corominas, A. Turon, J. Reinoso, E. Casoni, M. Paggi, J. A. Mayugo, A phase field approach enhanced with a cohesive zone model for modeling delamination induced by matrix cracking, *Computer Methods in Applied Mechanics and Engineering* 358 (2020) 112618.
- [9] W. Tan, E. Martínez-Pañeda, Phase field fracture predictions of microscopic bridging behaviour of composite materials, *Composite Structures* 286 (2022) 115242.
- [10] M. Simoes, E. Martínez-Pañeda, Phase field modelling of fracture and fatigue in Shape Memory Alloys, *Computer Methods in Applied Mechanics and Engineering* 373 (2021) 113504.
- [11] M. Simoes, C. Braithwaite, A. Makaya, E. Martínez-Pañeda, Modelling fatigue crack growth in Shape Memory Alloys, *Fatigue & Fracture of Engineering Materials & Structures* 45 (2022) 1243–1257.
- [12] W. Tan, E. Martínez-Pañeda, Phase field predictions of microscopic fracture and R-curve behaviour of fibre-reinforced composites, *Composites Science and Technology* 202 (2021) 108539.
- [13] P. K. A. V. Kumar, A. Dean, J. Reinoso, P. Lenarda, M. Paggi, Phase field modeling of fracture in Functionally Graded Materials: G -convergence and mechanical insight on the effect of grading, *Thin-Walled Structures* 159 (2021) 107234.
- [14] P. Carrara, M. Ambati, R. Alessi, L. De Lorenzis, A framework to model the fatigue behavior of brittle materials based on a variational phase-field approach, *Computer Methods in Applied Mechanics and Engineering* 361 (2020) 112731.

- [15] Z. Khalil, A. Y. Elghazouli, E. Martínez-Pañeda, A generalised phase field model for fatigue crack growth in elastic – plastic solids with an efficient monolithic solver, *Computer Methods in Applied Mechanics and Engineering* 388 (2022) 114286.
- [16] E. Martínez-Pañeda, A. Golahmar, C. F. Niordson, A phase field formulation for hydrogen assisted cracking, *Computer Methods in Applied Mechanics and Engineering* 342 (2018) 742–761.
- [17] J.-Y. Wu, T. K. Mandal, V. P. Nguyen, A phase-field regularized cohesive zone model for hydrogen assisted cracking, *Computer Methods in Applied Mechanics and Engineering* 358 (2020) 112614.
- [18] J.-Y. Wu, V. P. Nguyen, C. T. Nguyen, D. Sutula, S. Sinaie, S. Bordas, Phase-field modelling of fracture, *Advances in Applied Mechanics* 53 (2020) 1–183.
- [19] P. K. Kristensen, C. F. Niordson, E. Martínez-Pañeda, An assessment of phase field fracture: crack initiation and growth, *Philosophical Transactions of the Royal Society A: Mathematical, Physical and Engineering Sciences* 379 (2021) 20210021.
- [20] A. A. Griffith, The Phenomena of Rupture and Flow in Solids, *Philosophical Transactions A*, 221 (1920) 163–198.
- [21] Y. Navidtehrani, C. Betegón, R. W. Zimmerman, E. Martínez-Pañeda, Griffith-based analysis of crack initiation location in a Brazilian test, *International Journal of Rock Mechanics and Mining Sciences* (in press) (2022).
- [22] C. G. Sammis, M. F. Ashby, The failure of brittle porous solids under compressive stress states, *Acta Metallurgica* 34 (3) (1986) 511–526.
- [23] G. A. Francfort, J.-J. Marigo, Revisiting brittle fracture as an energy minimization problem, *Journal of the Mechanics and Physics of Solids* 46 (8) (1998) 1319–1342.
- [24] B. Bourdin, G. A. Francfort, J.-J. Marigo, Numerical experiments in revisited brittle fracture, *Journal of the Mechanics and Physics of Solids* 48 (4) (2000) 797–826.
- [25] H. Amor, J. J. Marigo, C. Maurini, Regularized formulation of the variational brittle fracture with unilateral contact: Numerical experiments, *Journal of the Mechanics and Physics of Solids* 57 (8) (2009) 1209–1229.

- [26] C. Miehe, M. Hofacker, F. Welschinger, A phase field model for rate-independent crack propagation: Robust algorithmic implementation based on operator splits, *Computer Methods in Applied Mechanics and Engineering* 199 (45-48) (2010) 2765–2778.
- [27] F. Freddi, G. Royer-Carfagni, Regularized variational theories of fracture: A unified approach, *Journal of the Mechanics and Physics of Solids* 58 (8) (2010) 1154–1174.
- [28] F. Freddi, G. Royer-Carfagni, Variational fracture mechanics to model compressive splitting of masonry-like materials, *Annals of Solid and Structural Mechanics* 2 (2-4) (2011) 57–67.
- [29] Y. S. Lo, M. J. Borden, K. Ravi-Chandar, C. M. Landis, A phase-field model for fatigue crack growth, *Journal of the Mechanics and Physics of Solids* 132 (2019) 103684.
- [30] J. Choo, W. C. Sun, Coupled phase-field and plasticity modeling of geological materials: From brittle fracture to ductile flow, *Computer Methods in Applied Mechanics and Engineering* 330 (2018) 1–32.
- [31] S. Zhou, X. Zhuang, T. Rabczuk, Phase field modeling of brittle compressive-shear fractures in rock-like materials: A new driving force and a hybrid formulation, *Computer Methods in Applied Mechanics and Engineering* 355 (2019) 729–752.
- [32] T. Wang, X. Ye, Z. Liu, D. Chu, Z. Zhuang, Modeling the dynamic and quasi-static compression-shear failure of brittle materials by explicit phase field method, *Computational Mechanics* 64 (6) (2019) 1537–1556.
- [33] L. D. Lorenzis, C. Maurini, Nucleation under multi-axial loading in variational phase-field models of brittle fracture, *International Journal of Fracture* (in press) (2022).
- [34] D. C. Drucker, W. Prager, Soil mechanics and plastic analysis for limit design, *Quarterly of Applied Mathematics* 10 (2) (1952) 157–165.
- [35] G. Del Piero, D. R. Owen, Structured deformations of continua, *Archive for Rational Mechanics and Analysis* 124 (2) (1993) 99–155.
- [36] Y. Navidtehrani, C. Betegón, E. Martínez-Pañeda, A unified Abaqus implementation of the phase field fracture method using only a user material subroutine, *Materials* 14 (8) (2021) 1913.
- [37] Y. Navidtehrani, C. Betegón, E. Martínez-Pañeda, A simple and robust Abaqus implementation of the phase field fracture method, *Applications in Engineering Science* 6 (2021) 100050.

- [38] D. D. Pollard, R. C. Fletcher, *Fundamentals of Structural Geology*, Cambridge University Press, 2010.
- [39] K. Hoshino, *Mechanical properties of Japanese Tertiary sedimentary rocks under high confining pressures*, Tech. rep. (1972).
- [40] J. Jaeger, N. Cook, R. Zimmerman, *Fundamentals of rock mechanics*, Blackwell Publishing, Oxford, UK, 2009.
- [41] R. A. Regueiro, R. I. Borja, Plane strain finite element analysis of pressure sensitive plasticity with strong discontinuity, *International Journal of Solids and Structures* 38 (21) (2001) 3647–3672.
- [42] F. Fei, J. Choo, A phase-field model of frictional shear fracture in geologic materials, *Computer Methods in Applied Mechanics and Engineering* 369 (2020) 113265.
- [43] A. Kumar, B. Bourdin, G. A. Francfort, O. Lopez-Pamies, Revisiting nucleation in the phase-Field approach to brittle fracture, *Journal of the Mechanics and Physics of Solids* 142 (2020) 104027.